



Hi-End-MAE: Hierarchical encoder-driven masked autoencoders are stronger vision learners for medical image segmentation

Fenghe Tang^{a,b}, Qingsong Yao^c, Wenxin Ma^{a,b}, Chenxu Wu^{a,b}, Zihang Jiang^{a,b,d,*}, S. Kevin Zhou^{a,b,d,e,*}

^aSchool of Biomedical Engineering, Division of Life Sciences and Medicine, University of Science and Technology of China (USTC), Hefei, Anhui, 230026, P.R. China

^bCenter for Medical Imaging, Robotics, and Analytic Computing & Learning (MIRACLE), Suzhou Institute for Advanced Research, USTC, Suzhou 215123, China

^cStanford University, Palo Alto, California, 94305, United State

^dState Key Laboratory of Precision and Intelligent Chemistry, USTC, Hefei, Anhui 230026, China

^eKey Laboratory of Intelligent Information Processing of Chinese Academy of Sciences (CAS), Institute of Computing Technology, CAS, Beijing, 100190, China

ARTICLE INFO

Article history:

Keywords: Masked Image Modeling, Encoder-driven Dense decoding, Medical Image Pre-training, Medical Image Segmentation

ABSTRACT

Medical image segmentation remains a formidable challenge due to the label scarcity. Pre-training Vision Transformer (ViT) through masked image modeling (MIM) on large-scale unlabeled medical datasets presents a promising solution, providing both computational efficiency and model generalization for various downstream tasks. However, current ViT-based MIM pre-training frameworks predominantly emphasize local aggregation representations in output layers and fail to exploit the rich representations across different ViT layers that better capture fine-grained semantic information needed for more precise medical downstream tasks. To fill the above gap, we hereby present **Hierarchical Encoder-driven MAE (Hi-End-MAE)**, a simple yet effective ViT-based pre-training solution, which centers on two key innovations: (1) Encoder-driven reconstruction, which encourages the encoder to learn more informative features to guide the reconstruction of masked patches; and (2) Hierarchical dense decoding, which implements a hierarchical decoding structure to capture rich representations across different layers. We pre-train Hi-End-MAE on a large-scale dataset of 10K CT scans and evaluated its performance across seven public medical image segmentation benchmarks. Extensive experiments demonstrate that Hi-End-MAE achieves superior transfer learning capabilities across various downstream tasks, revealing the potential of ViT in medical imaging applications. The code is available at: <https://github.com/FengheTan9/Hi-End-MAE>.

© 2025 Elsevier B. V. All rights reserved.

1. Introduction

Deep learning demonstrates remarkable advancements in medical image analysis (Zhou et al., 2023c); however, it's significantly hindered by the labor-intensive and time-consuming annotations by clinicians and experts (Zhang et al., 2023). Especially in 3D medical image segmentation, the limited annotated data

presents significant challenges for medical tasks (Taleb et al., 2020; Ma et al., 2021b; Luo et al., 2022). To alleviate this burden, a branch of self-supervised learning (SSL) methods are developed to pre-train the vision encoder on massive unlabeled data using proxy tasks (Chen et al., 2020; He et al., 2020a; Caron et al., 2021; He et al., 2022) and transfer it to downstream tasks. This paradigm presents a promising solution in label-efficient learning (Zhou et al., 2021; Wu et al., 2024; Tang et al., 2024).

Nevertheless, given the constraints of computational resources and increase in the amount of unlabeled medical data, pre-

*Corresponding authors: skevinzhou@ustc.edu.cn (S Kevin Zhou) and jzh0103@ustc.edu.cn (Z.H. Jiang).

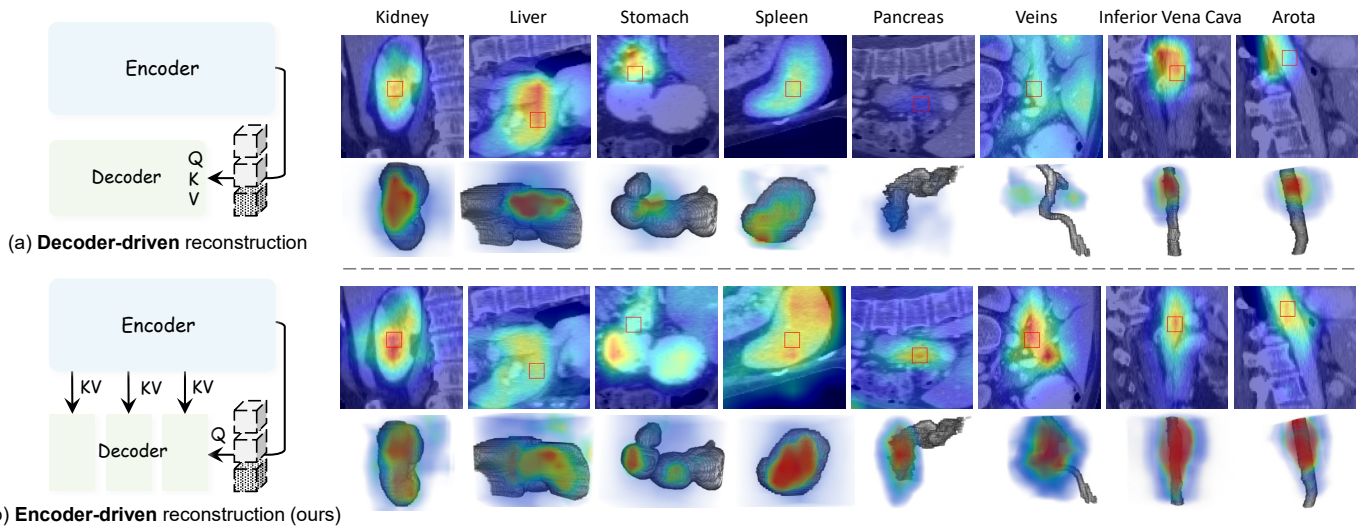


Fig. 1: Decoder-driven vs. encoder-driven reconstruction. Conventional MAE is based on (a) decoder-driven reconstruction and Hi-End-MAE is based on (b) encoder-driven reconstruction. The slice-based (the first row) and volume-based (the second row) attention maps for query patches (red box) on different anatomical structures in the last layer of ViT, pre-trained by MAE and Hi-End-MAE, are visualized. The attention maps of MAE tend to attention on limited local contexts while those of Hi-End-MAE tend to be of more complete anatomical contexts, which are more instrumental to medical image segmentation.

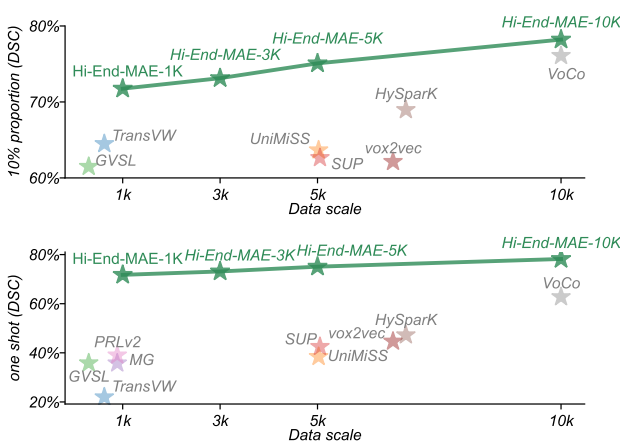


Fig. 2: Performance comparisons against well-known medical self-supervised learning method using different pre-training data scales. Top figure represents the results fine-tuned by 10% proportion of data, while the bottom figure represents fine-tuning with only one single 3D volume (one-shot).

training on large-scale 3D medical datasets poses significant challenges. This limitation has driven the need for resource-efficient and performance-scaling pre-training frameworks. In this context, a representative Masked Image Modeling (MIM) technique, Masked Autoencoder (MAE) (He et al., 2022), has emerged as a promising solution, which pre-trains Vision Transformer (ViT) (Dosovitskiy, 2020) by handling only a small subset of visible patches. This computationally efficient approach offers significant advantages for pre-training on large-scale 3D medical datasets (Chen et al., 2023a). However, the MAE framework imposes architectural constraints, requiring implementation through token-independent vanilla ViT architectures to boost pre-training efficiency. Compelling evidence from medical segmentation benchmarks reveals a fundamental limitation: segmentation networks built upon vanilla ViT backbones exhibit inferior performance compared to convolutional neural network (Ronneberger et al., 2015; Roy et al., 2023) or hybrid network (Tang et al., 2024). This performance gap originates from ViT’s intrinsic lack of spatial inductive biases — a criti-

cal shortcoming that becomes acutely detrimental when trained from scratch with limited annotated datasets (Hatamizadeh et al., 2022; Tang et al., 2022; Ronneberger et al., 2015; Roy et al., 2023; Tang et al., 2024). These factors lock the potential of ViT in medical image analysis.

The success of pre-trained Vision Transformer (ViT) in natural image processing (Caron et al., 2021; He et al., 2022) has motivated us to investigate its potential in medical vision tasks. Recent study reveal that masked image modeling (MIM) is inherently suited for low-level tasks as it effectively learns localized attention patterns that compensate for the limited inductive bias in ViT (Zhang et al., 2022a). Crucially, while pre-trained ViTs exhibit remarkable few-shot learning capabilities in natural image (Caron et al., 2021; He et al., 2022; Xie et al., 2022b; Bao et al., 2021), this generalization capacity remains underexplored in medical domains, which is essential for tackling segmentation tasks with label-scarcity.

Most advanced MIM methods designed for ViT, such as MAE, are tailored for natural images (He et al., 2022; Zhou et al., 2023b; Chen et al., 2024a; Dong et al., 2023; Xie et al., 2022b), where separate encoder and decoder are employed for representation and reconstruction. We categorize this series of methods as **decoder-driven reconstruction** (Fig. 1 (a)). Although this approach partially liberates the encoder’s representational capacity, the decoder still plays a crucial role in the reconstruction (Chen et al., 2024a), thus it does not perform well enough in medical image pre-training. As shown in Fig. 1, when visualizing the attention map at anatomies, we observe that MAE’s local query attention demonstrates limited adaptability across diverse anatomical contexts (*e.g.*, limited tubular and clustered attention patterns). We believe that this limitation likely stems from the MAE’s architectural constraints in capturing hierarchical medical semantics; specifically, they fail to adequately leverage high-quality, rich representations across ViT’s different layers during pre-training (shown in Fig. 6 and Fig. 7). Unlike conventional medical architectures (*e.g.*, U-Net (Ronneberger et al., 2015) and its variants (Roy et al., 2023; Hatamizadeh et al.,

2022; Tang et al., 2022)) that systematically leverage multi-scale feature learning through dense skip-connections, ViT implementations under typical MIM frameworks tend to prioritize local aggregation representation in the output layer, which might miss the potential gain brought by different layer rich anatomical structure information gains (shown in Fig. 5).

Based on the above limitation, a natural insight arises: *Is it possible to introduce efficient hierarchical local representation learning in MIM by solving proxy reconstruction tasks?* Different from the previous decoder-driven reconstruction, we try to introduce a simple yet effective **Hierarchical Encoder-driven dense-decoding architecture (Hi-End-MAE)** to solve this problem (shown in Fig. 1 (b)). There are two key innovative ideas behind Hi-End-MAE: (i) **Encoder-driven reconstruction**: utilizing decoder tokens to query visible encoded representations efficiently. The attention-weighted value further reconstructs the masked patches. This mechanism reduces the role of the decoder for reconstruction and directly establishes the relationship between representation quality and reconstruction ability, which makes the encoder learn stronger representation (encoder token values in Fig. 6 and Fig. 7). (ii) **Hierarchical dense decoding**: performing densely bottom-up hierarchical decoding to learn more informative anatomical patterns between different layers. During bottom-up encoder-driven dense decoding, Hi-End-MAE progressively reduces the decoder’s workload, which compels the encoder to learn informative, hierarchical representations to compensate for decoding information loss.

Compared to other medical SSL methods, our Hi-End-MAE not only learns higher-quality local representations, compensating the inherent inductive bias limitations of ViT, but also captures localized anatomical patterns across different layers, which are crucial for medical imaging tasks and friendly for up-downstream alignment. Furthermore, by using visible encoder tokens for decoding, our Hi-End-MAE is faster and stronger than MAE, making it well-suited for large-scale datasets pre-training. Through an extensive empirical evaluation across seven downstream medical datasets, we demonstrate that:

- Encoder-driven reconstruction in Hi-End-MAE could learn strong representations by solving proxy reconstruction tasks (Fig. 3), which outperforms other well-known medical SSL methods in one-shot segmentation tasks across six medical datasets (Fig. 2 (top) and Table 2) and different proportion fine-tuning on three medical datasets (Fig. 2 (bottom) and Table 3).
- Benefiting from hierarchical dense decoding, Hi-End-MAE learns richer localized anatomical representations across different layers than MAE (Fig. 6 and Fig. 7). Token-query-based attention map visualization also reveals that Hi-End-MAE could learn strong local patterns on specific organs, such as tubular attention and clustered attention (Fig. 1).
- Hi-End-MAE is also generalizable and efficient. The robust local patterns learned by Hi-End-MAE can effectively generalize to other modalities, such as MRI (Table 4). Additionally, thanks to encoder-driven reconstruction, Hi-End-MAE requires less computational cost than MAE (Table 6 and Table 7). This reduction in computation is linearly

related to the mask ratio, which greatly reduces the computational cost of large-scale 3D medical image pre-training while achieving powerful medical representations.

2. Related Works

2.1. Masked image modeling

Driven by BERT (Bao et al., 2021), masked image modeling (MIM) aims to remove or corrupt portions of the visual input and learn to predict the corrupted ones (Pathak et al., 2016; Xie et al., 2022b; He et al., 2022; Tian et al., 2023; Assran et al., 2022b; Chen et al., 2024a; Dong et al., 2023). These approaches have been studied to reveal their ability to learn local attention patterns (Zhang et al., 2022a) and demonstrate better transferability to downstream tasks, such as segmentation and detection (He et al., 2022; Xie et al., 2022b; Chen et al., 2024b; Tian et al., 2023; Tang et al., 2024). The most representative of these methods is Masked Autoencoders (MAE) (He et al., 2022), which achieves efficient pre-training by dropping masked tokens. Although MAE uses an asymmetric design for reconstruction, the decoder still plays a significant role in reconstruction, limiting the quality of representation learning (Chen et al., 2024a). Despite recent efforts (Chen et al., 2024a; Dong et al., 2023) to address this issue, they overlook the importance of different layer informative anatomical representation learning in visual pre-training tasks (Tian et al., 2023; Tang et al., 2024) and struggle to balance both efficiency and representational capability.

Given the importance of enhancing localized anatomical representation learning, the core idea of our approach is integrating hierarchical encoder-driven reconstruction into the decoding process, reducing the decoder’s workload in reconstruction to compel the encoder to assume a greater role in the reconstruction task.

2.2. Self-supervised learning for medical imaging.

Due to the scarcity of labeled medical images, self-supervised learning for medical images is a promising task (Li et al., 2023). Existing medical SSL methods are mainly based on contrastive learning, conducted with strong data augmentation *e.g.*, rotate (Tang et al., 2022; Tao et al., 2020) and multi-view crops (Zhou et al., 2023a; Xie et al., 2022a; Wu et al., 2024; He et al., 2023; Goncharov et al., 2023). However, most of these learn modality-specific high-level semantic representations (Assran et al., 2022b), which introduce strong biases in downstream tasks with different data distributions (Zhang et al., 2023; Assran et al., 2022a). In contrast, introducing MIM methods in medical image pre-training (Chen et al., 2023a; Zhou et al., 2023b; Tang et al., 2024) presents a promising avenue for addressing the above challenges (Li et al., 2023; Chen et al., 2023a). However, most of these methods rarely prioritize the learning of anatomical semantics and downstream adaptation, both of which are crucial for medical visual tasks.

In this paper, we propose a simple yet effective MIM method. Unlike previous works, we emphasize the importance of enhancing the encoder’s localized anatomical representation learning and downstream adaptability. By leveraging the encoder’s localized anatomical representations for dense decoding, our

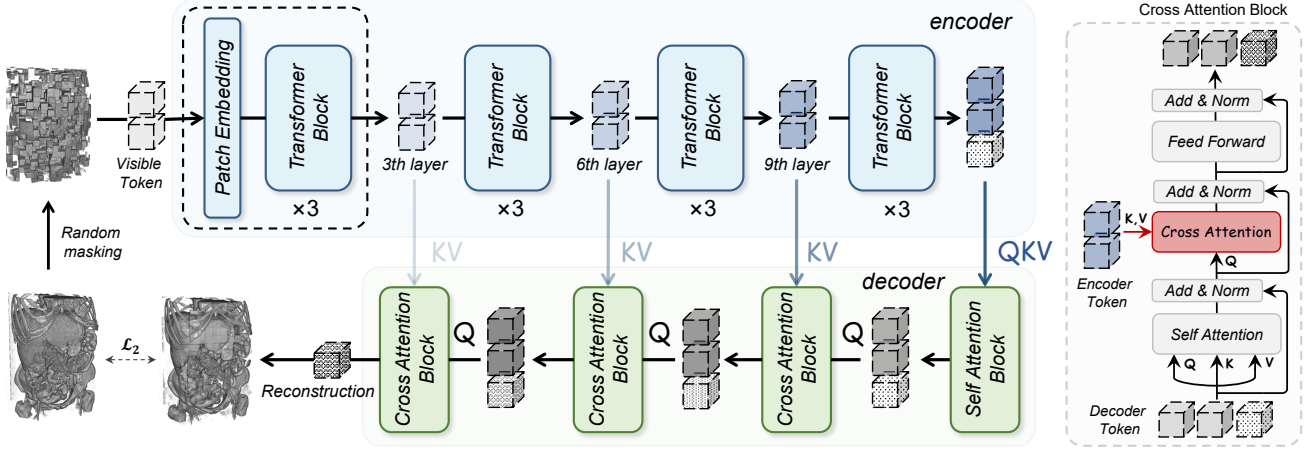


Fig. 3: **The overall framework of Hi-End-MAE.** The Encoder-driven Dense Decoding architecture uses encoder representations to guide the decoder bottom-up dense reconstruction. The encoder (blue) is a Vision Transformer (ViT), which only processes the visible patches (blue cube). The decoder (green) incorporates a cross-attention mechanism, feeding in a full set of token *i.e.* visible token (grey cube) and learnable masked token (mosaic cube) to query the encoder representation (blue arrow) for encoder-driven reconstruction.

approach not only minimizes the role of the decoder in reconstruction, unleashing the potential of the encoder in medical visual learning, but also enables seamless adaptation of the encoder to downstream tasks.

3. Methodology

The overall framework of Hi-End-MAE is illustrated in Fig. 3, which consists of two components: The **encoder** for localized anatomical representation across different layers and the **hierarchical encoder-driven dense decoder** for reconstruction.

3.1. Masked encoding

Tokenify and masking. We first tokenize the input 3D volume $x \in \mathbb{R}^{H \times W \times D}$ into a sequence of N volume patch tokens $\{x_i\}_{i=1}^N$, $x_i \in \mathbb{R}^{T \times P^3}$, where P is patch size, $T = HWD/P^3$ is number of tokens. Following the MAE (He et al., 2022), we mask out a large ratio (γ) of patches and feed the visible patches $\{x_j^v\}_{j=1}^{(1-\gamma)N}$ into the encoder.

Masked encoding. The encoder \mathcal{F} maps the visible patches x^v to multi-layer embedding features $\{Z_l^v\}_{l=1}^L$. We use ViT to form our encoder, which consists of L Transformer layers. It first embeds the visible tokens x^v by linear projection as token embeddings and adds the 3D positional embeddings followed by (Zhou et al., 2023b).

3.2. Hierarchical encoder-driven dense decoding

Unlike previous methods (He et al., 2022; Zhou et al., 2023b; Chen et al., 2024a), our proposed Hi-End-MAE fully utilizes encoder representations to guide the decoder for bottom-up dense reconstruction. The decoder \mathcal{D} consists of a self-attention block and B cross-attention blocks, which map the mask query token to the pixel space. We feed a full set of tokens $X_{\mathcal{D}} = \{x_i^{\mathcal{D}}\}_{i=1}^N$, consisting of last layer encoder tokens and learnable mask tokens with adding decoding position embeddings, into the decoder. Before encoder-driven reconstruction, we employ a few self-attention layers for early decoding adaption.

Encoder-driven reconstruction. To enable encoder-guided reconstruction which further enhances the encoder representation capacity, we introduce the cross-attention mechanism into the decoding process. Specifically, the decoding tokens ($Q_{\mathcal{D}}$) query visible encoder representations ($V_{\mathcal{F}}$) (blue arrow in Fig. 3), and then the queried values ($O_{\mathcal{D}}$) (grey and mosaic cube in Fig. 3) are used for the next stage decoding. Under encoder-driven reconstruction, the reconstruction quality directly depends on the encoder representation quality (V). This operation compels the encoder to learn stronger representations to compensate for the loss of reconstruction information. It can be represented as:

$$\text{Attention} = \text{Softmax}\left(\frac{QK^T}{\sqrt{d_k}}\right)V \quad (1)$$

$$\check{X}_{\mathcal{D}} = \text{Attention}(Q_{\mathcal{D}}, K_{\mathcal{D}}, V_{\mathcal{D}}) + X_{\mathcal{D}} \quad (2)$$

$$X_{\mathcal{F}2\mathcal{D}} = \text{Attention}(\check{Q}_{\mathcal{D}}, K_{\mathcal{F}}, V_{\mathcal{F}}) + \check{X}_{\mathcal{D}} \quad (3)$$

$$O_{\mathcal{D}} = \text{FeedForward}(X_{\mathcal{F}2\mathcal{D}}) + X_{\mathcal{F}2\mathcal{D}} \quad (4)$$

where the Eqs. (2) and (3) represent self-attention and cross-attention, respectively. $Q_{\mathcal{D}}$, $K_{\mathcal{D}}$, $V_{\mathcal{D}}$ and $\check{Q}_{\mathcal{D}}$ are linear projection from $X_{\mathcal{D}}$ and $\check{X}_{\mathcal{D}}$, respectively. Key ($K_{\mathcal{F}}$) and value ($V_{\mathcal{F}}$) in Equ.3 are linear projection from Z^v . $O_{\mathcal{D}}$ is the output queries. d_k is the feature dimension of K .

Hierarchical dense decoding. Considering the importance of localized anatomical representations across different layer for medical segmentation tasks, we introduce hierarchical bottom-up dense decoding. Specifically, in the bottom-up decoding process, the decoding at different stages queries the corresponding encoding representation (blue arrow in Fig. 3). It can be represented as:

$$X_{\mathcal{F}2\mathcal{D}}^{b,l} = \text{Attention}(\check{Q}_{\mathcal{D}}^b, K_{\mathcal{F}}^l, V_{\mathcal{F}}^l) + \check{X}_{\mathcal{D}}^b \quad (5)$$

where the $\check{X}_{\mathcal{D}}^b$, $b \in \{1, 2, \dots, B\}$ is the b -th stage decoding token. $\check{Q}_{\mathcal{D}}^b$ is query token linear projected from $\check{X}_{\mathcal{D}}^b$. $K_{\mathcal{F}}^l$ and $V_{\mathcal{F}}^l$ are linear projected by the correspond l -th layer encoder feature. Given

that dense decoding is a bottom-up decreasing information process, the closer to the output, the less representation information is supported by the encoder feature values (lighter arrow colors indicating weaker representations in Fig. 3), which compels the encoder to learn stronger and richer localized anatomical representations.

Reconstruction and loss. Followed by MAE (He et al., 2022; Zhou et al., 2023b), we use a linear projection layer for the final reconstruction and optimize a mean square error loss (\mathcal{L}_2) for masked region reconstruction.

Quantitative evaluation of encoder representation. Followed previous works (Zhang et al., 2022b; Park et al., 2024; Zhang et al.), we use singular values and effective rank (Roy and Vetterli, 2007) to quantify our encoder representation ability.

Given the matrix $A \in \mathbb{R}^{m \times n}$ and its singular values $\{\sigma_i\}_{i=1}^{\min(m,n)}$, the effective rank $\rho(A)$ is defined as:

$$\rho(A) = - \sum_{i=1}^{\min(m,n)} \bar{\sigma}_i \log(\bar{\sigma}_i) \quad (6)$$

where $\bar{\sigma}_i = \sigma_i / \sum_k \sigma_k$ is i -th normalized singular value. In this paper, matrix A represents the attention values (V) of each encoder layer.

Computational complexity of encoder-driven reconstruction.

Conventional decoder-driven reconstruction methods perform self-attention over the full set of N tokens, resulting in quadratic complexity $O(N^2 d_k)$, where N is the total number of tokens and d_k denotes the feature dimension. On the contrary, our proposed decoder-driven reconstruction could further reduce complexity by querying only visible encoded tokens. Specifically, only visible encoder tokens as Key ($K_{\mathcal{F}}$) and Value ($V_{\mathcal{F}}$) are participated in calculation, with the preserved token count $M = N \cdot (1 - \gamma)$, where $\gamma \in (0, 1)$ is the masking ratio. This reduces the complexity of computing the attention similarity matrix from $O(N^2 d_k)$ to $O(NM d_k) = O(N^2(1 - \gamma)d_k)$. For an encoder-driven reconstruction layer, the total complexity is given as:

$$O_{\text{total}} = O(N^2(1 - \gamma)d_k) + O(Nd_k^2). \quad (7)$$

Note that the first term in Eq. (7) is dominant. In our experiment, we set $\gamma = 0.75$, which means significant saving in computation in practice.

4. Experiments

4.1. Datasets

Pre-training datasets. As shown in Table 1, a total of 13 public CT datasets, consisting of 9995 ($\approx 10k$) CT scans, are curated to form our pre-training dataset, including BTCV (Landman et al., 2015), Sliver07 (Heimann et al., 2009), CT-ORG (Rister et al., 2020), FLARE’22 (Ma et al., 2023), CHAOS (Kavur et al., 2021), NaH-Seg (Podobnik et al., 2023), KiPA22 (He et al., 2021, 2020b; Shao et al., 2011, 2012), COVID-19 (Ma et al., 2021a), Pancreas-CT (Roth et al., 2016), LiTS (Bilic et al., 2023), AbdomenCT-1k (Ma et al., 2021b), LUNA16 (Setio et al., 2017), and AbdomenAtlasMini 1.0 (Li et al., 2024). Existing annotations or labels are not utilized from these datasets during pre-training. The pre-train datasets are interpolated to the

Table 1: Overview of pre-train and downstream dataset.

Dataset	# of volumes	Pre-train	Downstream
BTCV	50	✓	✓
Sliver07	20	✓	✓
CT-ORG	140	✓	✓
FLARE’22	2300	✓	✓
CHAOS	40	✓	
HaN-Seg	42	✓	
KiPA22	70	✓	
COVID-19	10	✓	
Pancreas-CT	82	✓	
LiTS	134	✓	
AbdomenCT-1k	1062	✓	
LUNA16	888	✓	
AbdomenAtlas 1.0	5195	✓	
WORD	150		✓
AMOS	600		✓
BraTS 21	1200		✓

isotropic voxel spacing of 1.5 mm. Intensities are scaled to $[-175, 250]$, then normalized to $[0, 1]$. We crop sub-volumes of $96 \times 96 \times 96$ voxels as input. Details are provided in the Appendix.

Downstream datasets. To evaluate the effectiveness of our method, we conduct downstream experiments on seven public datasets for medical image segmentation (Lay et al., 2013), e.g., BTCV (Landman et al., 2015), CT-ORG (Rister et al., 2020), Sliver07 (Heimann et al., 2009), WORD (Luo et al., 2022), AMOS (Ji et al., 2022), FLARE’22 (Ma et al., 2023) and BraTS21 (Baid et al., 2021). To better assess the representation capacity of the pre-trained model, we employ the first six datasets for one-shot segmentation tasks. Additionally, following previous works (Huang et al., 2024; Yang et al., 2022; Gowda and Clifton, 2024; Isensee et al., 2024), we selected AMOS (Ji et al., 2022), FLARE’22 (Ma et al., 2023) and BTCV (Landman et al., 2015) datasets with official training-validation split for downstream experiments with 1%, 10% and 100% data proportions. To assess the model’s cross-modality generalization capability, we transfer the pre-trained model from the CT domain to the MRI (i.e. adapt in BraTS 21 (Baid et al., 2021)) for further evaluation. We adopt consistent settings as previous works (Hatamizadeh et al., 2022; Tang et al., 2022; Wu et al., 2024). More pre-training details are provided in the Appendix.

4.2. Implementation details

Experiment settings. Following previous works (Zhou et al., 2023b; Chen et al., 2023b; Tang et al., 2024), we adopt UNETR (Hatamizadeh et al., 2022) as the downstream networks. To achieve upstream-downstream alignment, we set three decoding stages, corresponding to the encoder representations at layers 3-th, 6-th, and 9-th, e.g. same skip-connection layers in UNETR, to guide decoder reconstruction. For pre-training tasks, we train with the AdamW optimizer, an initial learning rate of $1e-4$, and a cosine-annealing scheduler for all experiments. The pre-training experiments use a batch size of 192 and train the model for 400K steps. For fair downstream comparisons, detailed training hyper-parameters settings for fine-tuning and inference are the same as previous works (Hatamizadeh et al., 2022; Tang et al., 2022; Wu et al., 2024; Tang et al., 2024). Details are provided in the Appendix.

Table 2: Comparison of different methods for one-shot segmentation on BTCV, CT-ORG, Sliver07, WORD, AMOS and FLARE’22. **val** (bold) / val (underline) : top method / second method. † denotes we utilize official pre-training weights.

Pretrain Method		# Volume	Dataset (DSC %)						Avg
Method	Network		BTCV	CT-ORG	Sliver07	WORD	AMOS	FLARE’22	
<i>Training from scratch</i>									
-	UNETR	WACV’22	24.27	49.08	80.87	30.89	10.06	26.30	36.91
-	SwinUNETR	CVPR’22	27.71	55.28	80.91	43.68	9.59	35.89	42.17
<i>General self-supervised methods</i>									
SparK	MedNeXt	ICLR’23	30.69	62.24	84.89	50.64	13.34	36.48	46.37
MAE	UNETR	CVPR’22	62.04	<u>69.75</u>	78.02	<u>69.06</u>	38.05	<u>62.35</u>	<u>63.21</u>
<i>Medical self-supervised methods</i>									
MG†	3D U-Net	MICCAI’20	29.27	51.12	67.40	27.95	11.67	27.30	35.78
TransVW†	3D U-Net	TMI’21	5.63	34.74	75.77	7.23	3.66	4.81	21.97
UniMiSS†	MiT	ECCV’22	32.95	60.24	75.96	23.03	13.46	24.92	38.42
SUP†	SwinUNETR	CVPR’22	28.75	56.72	78.99	46.95	9.94	33.72	42.51
PRLv2†	3D U-Net	TPAMI’23	24.01	55.86	83.35	31.69	11.54	27.71	39.02
GVSL†	3D U-Net	CVPR’23	24.86	54.57	60.53	37.87	10.84	26.33	35.83
vox2vec†	3D U-Net	MICCAI’23	35.29	62.91	72.94	49.37	13.44	34.11	44.67
HySparK†	MedNeXt + ViT	MICCAI’24	35.81	60.83	80.61	53.27	15.31	37.54	47.22
VoCo†	SwinUNETR	CVPR’24	<u>63.33</u>	65.12	<u>87.43</u>	64.24	<u>38.80</u>	57.66	62.76
Hi-End-MAE	UNETR	ours	69.59	71.09	91.88	73.52	46.21	63.22	69.25

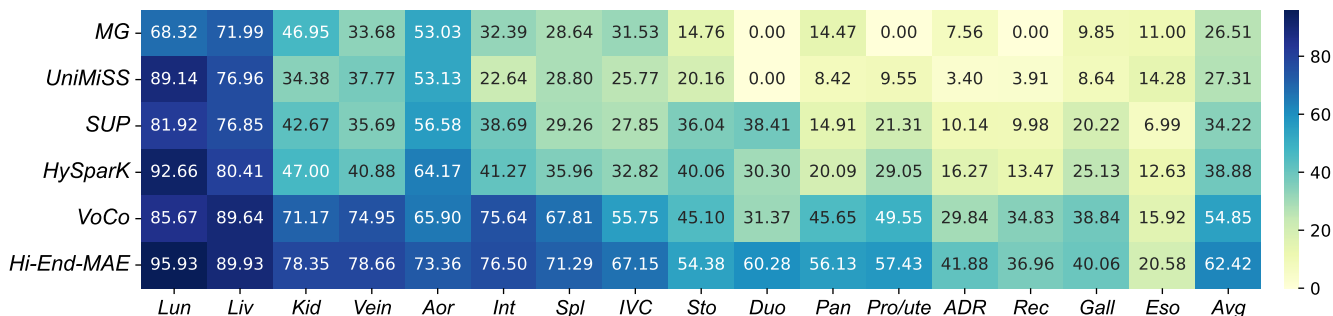


Fig. 4: Comparative analysis one-shot segmentation results across 16 targets in terms of DSC (%) performance. The abbreviations Lun, Liv, Kid, Vein, Aor, Int, Spl, IVC, Sto, Duo, Pan, Pro/ute, ADR, Rec, Gall and Eso correspond to Lung, Liver, Kidney, Veins, Aorta, Intestine, Spleen, Inferior Vena Cava, Stomach, Duodenum, Pancreas, Prostate/Uterus, Adrenal Gland, Rectum, Gallbladder and Esophagus, respectively.

Comparison methods. We select both general and medical self-supervised methods for a comprehensive comparison. First, we pre-train and compare with the well-known MIM method MAE (He et al., 2022; Zhou et al., 2023b) and SparK (Tian et al., 2023) with the same experiment settings. In addition, we choose nine advanced and well-known medical self-supervised methods: Models Genesis (MG) (Zhou et al., 2021), TransVW (Haghighi et al., 2021), UniMiSS (Xie et al., 2022a), Swin UNETR Pre-trained method (SUP) (Tang et al., 2022), PRLv2 (Zhou et al., 2023a), GVSL (He et al., 2023), vox2vec (Goncharov et al., 2023), HySparK (Tang et al., 2024) and VoCo¹ (Wu et al., 2024). To ensure a fair comparison, we load the official pre-trained weights for all medical SSL methods before fine-tuning.

4.3. Experiments on downstream tasks

Overall one-shot medical segmentation. We first conduct one-shot segmentation on six datasets, as shown in Table 2. Our method substantially outperforms both general and medical self-supervised approaches, achieving a DSC score of 69.25%, at

least 6.04% higher than all compared methods. The Hi-End-MAE pre-training yields a 32.34% improvement over training from scratch. Compared to the recent contrastive-based method VoCo (Wu et al., 2024), which uses similarly-sized pre-training datasets (10k), Hi-End-MAE shows consistent improvements of 6.26%, 5.97%, 4.45%, and 5.56% on BTCV (Landman et al., 2015), CT-ORG (Rister et al., 2020), Sliver07 (Heimann et al., 2009), and FLARE’22 (Ma et al., 2023), respectively. Notably, on datasets unseen during pre-training, e.g., WORD (Luo et al., 2022) and AMOS (Ji et al., 2022), our method demonstrates promising performance, higher than VoCo with DSC of 9.28% and 7.41%, respectively. Additionally, it can be observed that apart from our method, which achieves a new state-of-the-art (SOTA) of 69.25%, another ViT pre-trained with MIM also demonstrates notable generalization benefits, with MAE achieving 63.21%.

Target-specific analysis and visualization. To comprehensively evaluate the advantages of Hi-End-MAE across different segmentation targets, we investigate the one-shot segmentation semantics results on six datasets. Comparative results are partially shown in Fig.4. Hi-End-MAE achieves optimal results for most organs. Compared to the recent SOTA method VoCo (Wu et al., 2024), Hi-End-MAE shows significant improvements across

¹official 10K ct-scan pre-training weights

Table 3: Comparison of different methods with different proportions on AMOS (Ji et al., 2022), FLARE’22 (Ma et al., 2023) and BTCV (Landman et al., 2015). We report the DSC (%) performance. **val** (bold) / val (underline) : top method / second method. † denotes we utilize official pre-training weights. ‡ denotes the results are copied from (Wu et al., 2024).

Pretrain Method	# Volume	AMOS				FLARE’22				BTCV				Avg
		1%	10%	100%	Avg	1%	10%	100%	Avg	1%	10%	100%‡	Avg	
<i>Training from scratch</i>														
UNETR	WACV’22	23.67	60.06	77.02	57.45	22.47	56.46	70.81	49.91	28.05	42.85	79.82	50.24	52.53
SwinUNETR	CVPR’22	28.94	63.45	82.51	58.30	35.89	63.38	75.38	58.21	27.71	51.33	80.53	53.19	56.56
<i>General self-supervised methods</i>														
SparK	ICLR’23	36.14	71.68	84.07	63.96	36.48	71.74	80.67	62.96	30.69	51.26	-	-	-
MAE	CVPR’22	54.67	72.94	83.61	70.40	<u>62.35</u>	77.01	82.56	<u>73.97</u>	62.04	75.01	-	-	-
<i>Medical self-supervised methods</i>														
MG†	MICCAI’20	25.72	46.94	62.99	45.21	27.30	48.18	57.33	44.27	29.27	38.04	81.45	49.58	56.97
TransVW†	TMI’21	18.72	66.91	82.58	56.06	4.81	62.07	75.78	47.55	5.63	8.42	-	-	-
UniMiSS†	ECCV’22	29.49	66.34	79.92	58.58	24.92	60.99	74.71	53.54	32.95	47.08	-	-	-
SUP†	CVPR’22	25.60	64.95	82.45	57.66	33.72	60.35	74.96	56.34	28.75	49.67	81.54	53.32	55.77
PRLv2†	TPAMI’23	21.07	39.07	54.14	38.09	27.71	42.97	54.29	41.65	24.01	30.48	81.74	45.41	41.71
GVSL†	CVPR’23	24.25	63.45	81.38	56.35	26.33	59.54	73.27	53.04	24.86	41.79	81.87	49.50	52.96
vox2vec†	MICCAI’23	32.76	62.30	74.78	56.61	34.11	61.99	70.33	55.47	35.29	51.77	-	-	-
HySparK†	MICCAI’24	34.50	64.32	85.58	61.46	37.54	73.60	82.35	64.49	35.81	51.54	-	-	-
VoCo†	CVPR’24	<u>55.81</u>	<u>73.34</u>	84.44	71.19	57.66	78.84	<u>83.12</u>	73.20	<u>63.33</u>	<u>77.85</u>	<u>83.85</u>	<u>75.01</u>	73.13
Hi-End-MAE	ours	60.35	75.84	<u>84.98</u>	73.72	63.22	80.58	84.20	76.00	69.59	78.56	84.53	77.56	75.72

Table 4: Experimental one-shot results on BRATS 21 (Baid et al., 2021). TC, WT, and ET denote the tumor core, whole tumor, and enhancing tumor, respectively. **val** (bold) / val (underline) : top method / second method. † denotes we utilize official pre-training weights.

Pretrain Method	# Backbone	TC	WT	ET	Avg
<i>Training from scratch</i>					
-	UNETR	49.72	54.82	56.27	53.60
-	SwinUNETR	50.44	57.81	<u>59.60</u>	55.95
<i>General self-supervised methods</i>					
MAE	UNETR	34.54	45.51	39.24	39.76
SparK	MedNeXt	44.04	65.52	44.90	51.49
<i>Medical self-supervised methods</i>					
MG†	3D U-Net	28.25	34.08	33.52	31.95
UniMiSS†	MiT	6.20	17.56	23.94	15.90
SUP†	SwinUNETR	49.96	53.51	56.65	53.37
GVSL†	3D U-Net	<u>54.11</u>	73.04	53.45	<u>60.20</u>
vox2vec†	3D U-Net	23.93	33.33	21.97	26.41
HySparK†	MedNeXt + ViT	40.05	44.36	46.98	43.79
VoCo†	SwinUNETR	40.76	53.12	55.41	49.76
Hi-End-MAE	UNETR	55.35	<u>68.25</u>	67.46	61.45

organs of different scales, *e.g.*, with enhancements of 28.91%, 10.48%, 10.26%, and 11.40% for the duodenum, pancreas, lung, and inferior vena cava, respectively. This indicates that Hi-End-MAE encourages the encoder to learn strong and rich localized anatomical representations. Additionally, we visualize segmentation results in Fig.8. Benefiting from high-quality localized anatomical representations, Hi-End-MAE achieves more complete and accurate segmentation results.

Comparison across various data proportions. Following previous works (Huang et al., 2024; Yang et al., 2022), we fine-tune pre-trained models on AMOS (Ji et al., 2022), FLARE’22 (Ma et al., 2023), and BTCV (Landman et al., 2015) using 1%, 10%, and 100% of the dataset, as shown in the Table 3. Hi-End-MAE achieves an average DSC score of 75.72% across various data proportions, clearly outperforming existing methods. Notably, our method surpasses the highest-performing compared method, VoCo, by 2.59%. In terms of the gains from pre-training, our backbone network UNETR achieves a substantial improvement of 23.19% compared to training from scratch (*e.g.*, 52.53% to 75.72%), whereas VoCo’s backbone SwinUNETR shows a gain

Table 5: The effect of mask ratios.

Mask Ratio	BTCV	CT-ORG	Sliver07	WORD	AMOS	FLARE’22	Avg
75%	69.59	71.09	91.88	73.52	46.21	63.22	69.25
80%	67.52	71.68	91.25	72.86	46.10	59.39	68.13
85%	66.43	69.04	87.81	70.94	41.32	61.89	66.23
90%	64.38	69.58	85.61	71.25	41.41	62.12	65.72
95%	64.63	70.67	83.14	67.35	32.19	61.72	63.28

of 16.57% compared to training from scratch (*e.g.*, 56.56% to 73.13%). These results prove that our improvement is consistent across different dataset proportions.

Generalization to MRI modalities. Our results prove that the performance gain of Hi-End-MAE is generalizable to other modalities. As shown in Table 4, we evaluate the downstream on a widely used MRI dataset, *e.g.* BraTS 21 (Baid et al., 2021). Hi-End-MAE achieves the highest DSC score, *e.g.* 61.45%, in one-shot segmentation, surpassing existing SOTA methods. Despite the significant differences in high-level semantics between MRI and CT, this generalization ability highlights that Hi-End-MAE effectively learns low-level representations that are independent of high-level semantics, thereby improving its performance across different modalities.

4.4. Analysis

Representation analysis. Following previous work (Roy and Vetterli, 2007; Zhang et al., 2022c), we analyze representational capability by calculating the distributions of effective ranks and singular values (Roy and Vetterli, 2007) for the attention values (V) across each transformer layer in both the MAE (He et al., 2022; Zhou et al., 2023b) and Hi-End-MAE encoders. Except for input-related shallow layers, Hi-End-MAE demonstrates a broader range of effective ranks and higher singular values are positively correlated with stronger representational capacity. The results for all transformer layers are shown in Fig.6 and Fig.7. In terms of effective rank (Fig.6), Hi-End-MAE exhibits a notable distribution shift compared to MAE, exhibiting a broader range of feature representations. Furthermore, Hi-End-MAE shows a shift towards higher singular values (Fig.7), indicating a greater presence of high-variance components, which contribute to more detailed and diverse representations.

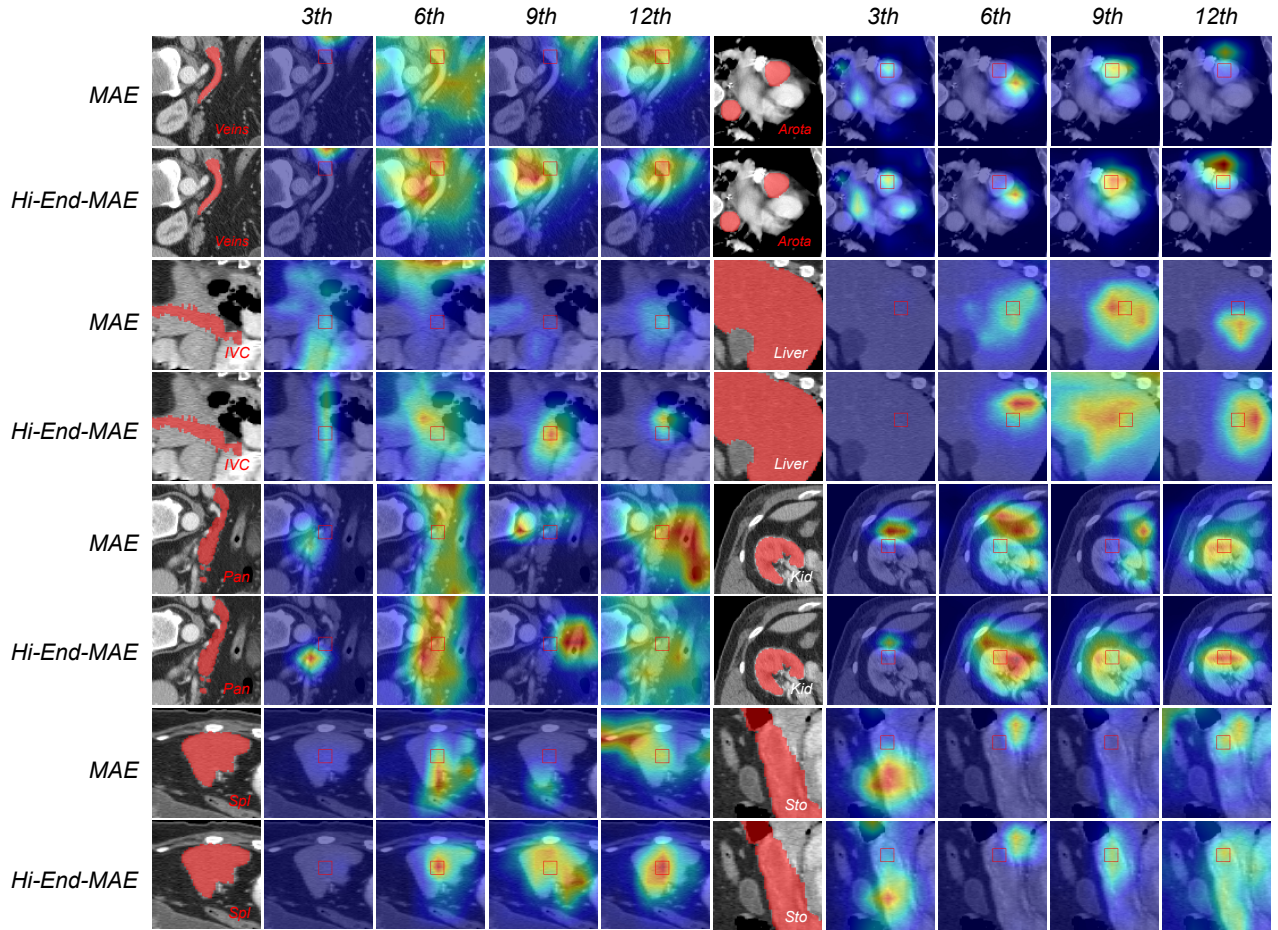


Fig. 5: Visualization of attention maps in the 3th, 6th, 9th, and 12th layers of ViT-B/12⁽¹⁵³⁶⁾ for query patches (red box) on different organs, pre-trained by MAE and Hi-End-MAE. The attention maps correspond to the same attention head in both MAE and Hi-End-MAE encoder.

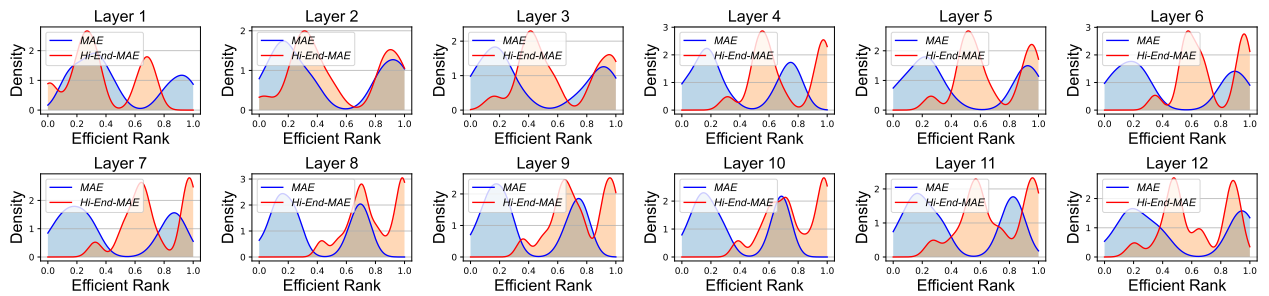


Fig. 6: Comparison effective rank (Roy and Vetterli, 2007) distribution of attention values (V) with MAE and Hi-End-MAE in ViT-B/12⁽¹⁵³⁶⁾. A rightward shift indicates a richer effective rank, reflecting more diverse data representations and a more uniform distribution. This enables the model to capture greater information from the feature space.

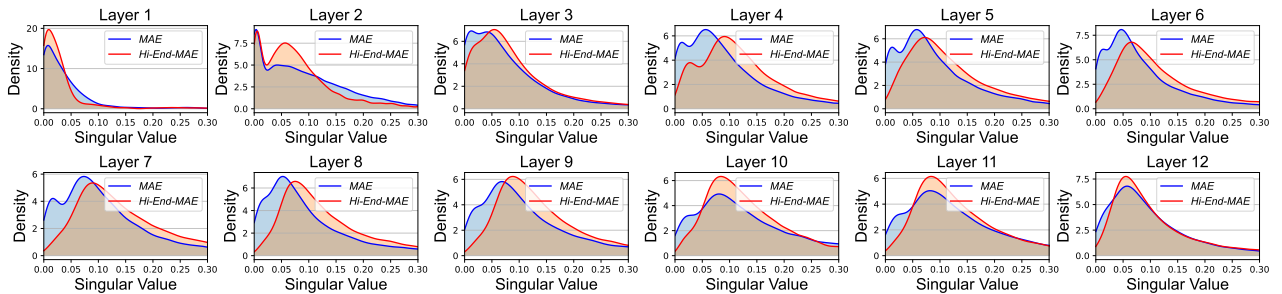


Fig. 7: Comparison singular values distribution of attention values (V) with MAE and Hi-End-MAE in ViT-B/12⁽¹⁵³⁶⁾. A rightward shift indicates higher variance, suggesting stronger generalization ability and more diversified data representation.

Table 6: Evaluation of encoder-driven reconstruction against decoder-driven reconstruction. We report the DSC score (%) on three datasets with various proportions. **val** (bold): top method.

Method	Encoder variants	Decoder FLOPS	AMOS				FLARE'22				BTCV				Avg	
			1%	10%	100%	Avg	1%	10%	100%	Avg	1%	10%	100%	Avg		
Decoder-driven reconstruction		16.44 G	58.84	75.74	84.80	73.56	63.33	78.67	83.80	72.08	66.85	78.36	83.20	76.13	73.92	
MAE	ViT-B/12 ⁽¹⁵³⁶⁾		Encoder-driven reconstruction		60.03	75.83	84.97	73.61	63.22	80.58	84.19	74.00	69.59	78.56		84.53
Hi-End-MAE	ViT-B/12 ⁽¹⁵³⁶⁾	10.69 G														

Table 7: Evaluation of dense-decoding components with different variants encoder. We report the one-shot DSC score (%) on six datasets. **val** (bold) / val (underline): top method / second method.

Encoder variants	Dense Decoding					Dataset						Avg
	w/o	stage3	stage2	stage1	FLOPS	BTCV	CT-ORG	Sliver07	WORD	AMOS	FLARE'22	
ViT-B/16 ⁽⁷⁶⁸⁾	-	-	-	-	-	24.27	49.08	80.87	30.89	10.06	26.30	36.91
	✓	-	-	-	3.51 G	62.04	69.75	78.02	69.06	38.05	62.35	63.21
	-	✓	✓	✓	2.38 G	63.21	70.84	80.30	66.32	38.55	60.83	63.34
ViT-B/16 ⁽¹⁵³⁶⁾	-	-	-	-	-	27.52	46.43	76.16	31.07	7.47	23.41	35.34
	✓	-	-	-	6.41 G	61.94	69.37	83.92	67.23	38.52	59.30	63.38
	-	✓	✓	✓	4.39 G	62.15	70.66	89.71	69.05	37.70	63.27	65.42
ViT-B/12 ⁽¹⁵³⁶⁾	-	-	-	-	-	28.05	52.11	80.62	34.79	11.04	27.94	39.09
	✓	-	-	-	16.44 G	66.78	71.38	<u>88.76</u>	71.68	39.62	63.33	66.92
	-	-	-	-	14.52 G	64.98	69.12	88.29	71.33	40.78	62.28	66.13
	-	-	✓	✓	12.61 G	<u>69.07</u>	<u>71.28</u>	86.46	<u>72.72</u>	<u>42.39</u>	64.41	<u>67.72</u>
	-	✓	✓	✓	10.69 G	69.59	<u>71.09</u>	91.88	73.52	46.21	<u>63.22</u>	69.25

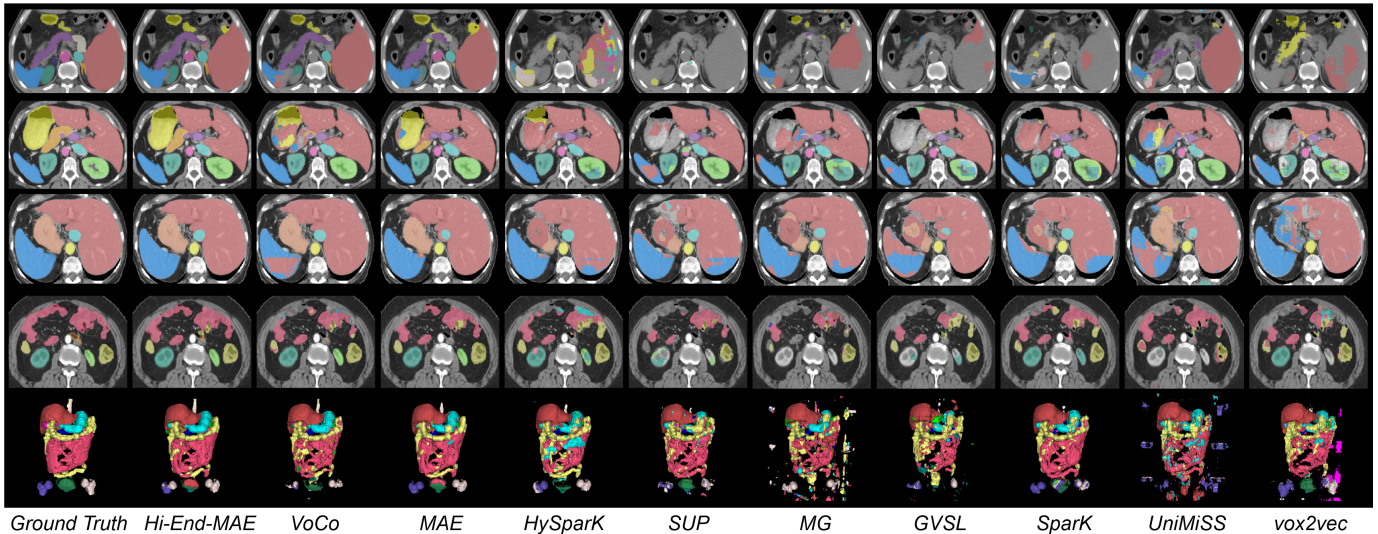


Fig. 8: Qualitative visualization of one-shot segmentation results for AMOS (Ji et al., 2022) (row 1), BTCV (Landman et al., 2015) (row 2), FLARE'22 (Ma et al., 2023) (row 3) and WORD (Luo et al., 2022) (row 4 and 5).

Local attention patterns. To intuitively demonstrate the specific representations learned by Hi-End-MAE, we visualize the slice-level (row 1) and volume-level (row 2) attention maps in Fig.1. These maps are generated by calculating the attention scores between a given query (highlighted in red boxes) and other patches. In contrast to decoder-driven methods, such as MAE, our encoder-driven Hi-End-MAE's self-attention maps focus more precisely on local patterns within specific organs, *e.g.*, tubular attention in structures like the aorta, inferior vena cava, and veins, as well as clustered attention in the liver, kidneys, and spleen. Then, we visualize the different attention heads from 3th, 6th, 9th, and 12th ViT layers. As evidenced in Fig.5, our Hi-End-MAE demonstrates markedly enhanced capability in anatomical attention across multiple ViT layers, producing more discriminative fine-grained feature essential for medical image segmentation. Empirical evidence indicates that Hi-End-MAE

empowers individual ViT tokens to achieve rich aggregation of local medical features, transfer into strong performance gains for pixel-level medical downstream tasks.

4.5. Ablations

We first analyze the effects of decoder-driven and encoder-driven reconstruction on AMOS (Ji et al., 2022), FLARE'22 (Ma et al., 2023), and BTCV (Ma et al., 2023) datasets with 1%, 10%, and 100% data proportions. Then, we conduct comprehensive ablation studies, across six datasets for one-shot segmentation, to evaluate dense decoder components, the mask ratios, and the scaling capabilities of ViT by Hi-End-MAE pre-training.

Encoder-driven against Decoder-driven reconstruction. We first explore the gains brought by our proposed encoder-driven reconstruction, as shown in Table 6. Our proposed method achieves better results, *e.g.*, 1.13% average DSC improve-

ment, and lower computational cost, *e.g.*, 34.97% computational cost reduced, than decoder-driven reconstruction across three datasets. This demonstrates that the encoder-driven reconstruction could enhance representation quality (Table 6) and learn localized anatomical representations (Fig. 6), benefiting various downstream tasks and highlighting the promising potential.

Dense decoder components. We further evaluate the effect of dense decoder number settings (B), *e.g.*, by replacing self-attention mechanism in original decoder with cross-attention in Hi-End-MAE across various encoder variants. As shown in Table 7, the results demonstrate that introducing the dense decoder in pre-training improves performance while reducing computational cost across all variants. Additionally, to assess the contribution of each block in different stages, we incrementally add dense decoder blocks from bottom to top in ViT-B/12⁽¹⁵³⁶⁾, achieving progressive gains in both performance and computational efficiency. With $B = 3$, we achieve the highest performance (*e.g.*, 69.25% DSC) and the lowest computational cost (*e.g.*, 10.69 GFLOPS). This suggests that progressive gains arise from the incremental addition of dense decoder blocks, which gradually reduces the decoder’s workload and compels the encoder to learn higher-quality, localized anatomical representations.

Scaling-up ViT in medical images. We evaluate the scalability of Hi-End-MAE with respect to both data size and model size. As shown in Fig. fig:vs, with different data scales (*e.g.*, 1K, 3K, 5K, 10K), Hi-End-MAE learns better representations than other medical SSL methods, achieving superior and scalable downstream performance. Specifically, performance increases from 71.75% to 78.21% for 10% fine-tuning and from 63.32% to 69.25% for one-shot segmentation as the data scale grows from 1K to 10K. Regarding model size, we compare ViT-B/16⁽⁷⁶⁸⁾, ViT-B/16⁽¹⁵³⁶⁾ and ViT-B/12⁽¹⁵³⁶⁾ with same-settings for pre-training. The results, presented in Table 7, show that Hi-End-MAE outperforms training from scratch (Table 7 row 1) and pre-training with MAE (Table 7 row 2), demonstrating better scalability, superior performance, and lower computational cost.

Mask ratio. We also conduct experiments with different mask ratios including 75%, 80%, 85%, 90% and 95%. Results are listed in Table 5. Our findings show that a 75% mask ratio yields better performance than higher mask ratios.

5. Conclusion

The necessity of low-level and high-quality localized anatomical representation learning prompts us to explore a novel architecture paradigm for fine-grained medical image pre-training. In this paper, we present Hi-End-MAE, a simple yet effective medical SSL framework. Different from previous decoder-driven reconstruction, Hi-End-MAE utilizes encoder-driven dense-decoding to gain high-quality medical representation. Specifically, it contains two parts: (1) encoder-driven reconstruction utilizing decoder tokens to query visible encoded representations and (2) Hierarchical dense decoding performing densely bottom-up hierarchical decoding to learn informative anatomical representations. Extensive experiments demonstrate Hi-End-MAE brings significant performance leaps in downstream tasks and

it reveals the encoder-driven reconstruction could learn strong localized anatomical representation across different ViT layers. We hope our encoder-driven paradigm could inspire more work to maximize the potential of masked image modeling in medical self-supervised learning tasks.

6. Acknowledgments

Supported by Natural Science Foundation of China under Grant 62271465, Suzhou Basic Research Program under Grant SYG202338, and Open Fund Project of Guangdong Academy of Medical Sciences, China (No. YKY-KF202206).

References

- Assran, M., Balestriero, R., Duval, Q., Bordes, F., Misra, I., Bojanowski, P., Vincent, P., Rabbat, M., Ballas, N., 2022a. The hidden uniform cluster prior in self-supervised learning. arXiv preprint arXiv:2210.07277 .
- Assran, M., Caron, M., Misra, I., Bojanowski, P., Bordes, F., Vincent, P., Joulin, A., Rabbat, M., Ballas, N., 2022b. Masked siamese networks for label-efficient learning, in: European Conference on Computer Vision, Springer. pp. 456–473.
- Baid, U., Ghodasara, S., Mohan, S., Bilello, M., Calabrese, E., Colak, E., Farahani, K., Kalpathy-Cramer, J., Kitamura, F.C., Pati, S., et al., 2021. The rsna-asnr-miccai brats 2021 benchmark on brain tumor segmentation and radiogenomic classification. arXiv preprint arXiv:2107.02314 .
- Bao, H., Dong, L., Piao, S., Wei, F., 2021. Beit: Bert pre-training of image transformers. arXiv preprint arXiv:2106.08254 .
- Bilic, P., Christ, P., Li, H.B., Vorontsov, E., Ben-Cohen, A., Kaissis, G., Szeskin, A., Jacobs, C., Mamani, G.E.H., Chartrand, G., et al., 2023. The liver tumor segmentation benchmark (lits). Medical Image Analysis 84, 102680.
- Caron, M., Touvron, H., Misra, I., Jégou, H., Mairal, J., Bojanowski, P., Joulin, A., 2021. Emerging properties in self-supervised vision transformers, in: Proceedings of the IEEE/CVF international conference on computer vision, pp. 9650–9660.
- Chen, T., Kornblith, S., Norouzi, M., Hinton, G., 2020. A simple framework for contrastive learning of visual representations, in: International conference on machine learning, PMLR. pp. 1597–1607.
- Chen, X., Ding, M., Wang, X., Xin, Y., Mo, S., Wang, Y., Han, S., Luo, P., Zeng, G., Wang, J., 2024a. Context autoencoder for self-supervised representation learning. International Journal of Computer Vision 132, 208–223.
- Chen, X., Ding, M., Wang, X., Xin, Y., Mo, S., Wang, Y., Han, S., Luo, P., Zeng, G., Wang, J., 2024b. Context autoencoder for self-supervised representation learning. International Journal of Computer Vision 132, 208–223.
- Chen, Z., Agarwal, D., Aggarwal, K., Safta, W., Balan, M.M., Brown, K., 2023a. Masked image modeling advances 3d medical image analysis, in: Proceedings of the IEEE/CVF Winter Conference on Applications of Computer Vision, pp. 1970–1980.
- Chen, Z., Agarwal, D., Aggarwal, K., Safta, W., Balan, M.M., Brown, K., 2023b. Masked image modeling advances 3d medical image analysis, in: Proceedings of the IEEE/CVF Winter Conference on Applications of Computer Vision, pp. 1970–1980.
- Clark, K., Vendt, B., Smith, K., Freymann, J., Kirby, J., Koppel, P., Moore, S., Phillips, S., Maffitt, D., Pringle, M., et al., 2013. The cancer imaging archive (tcia): maintaining and operating a public information repository. Journal of digital imaging 26, 1045–1057.
- Dong, X., Bao, J., Zhang, T., Chen, D., Zhang, W., Yuan, L., Chen, D., Wen, F., Yu, N., Guo, B., 2023. Peco: Perceptual codebook for bert pre-training of vision transformers, in: Proceedings of the AAAI Conference on Artificial Intelligence, pp. 552–560.
- Dosovitskiy, A., 2020. An image is worth 16x16 words: Transformers for image recognition at scale. arXiv preprint arXiv:2010.11929 .
- Goncharov, M., Soboleva, V., Kurmukov, A., Pisov, M., Belyaev, M., 2023. vox2vec: A framework for self-supervised contrastive learning of voxel-level representations in medical images, in: International Conference on Medical Image Computing and Computer-Assisted Intervention, Springer. pp. 605–614.

- Gowda, S.N., Clifton, D.A., 2024. Masks and manuscripts: Advancing medical pre-training with end-to-end masking and narrative structuring, in: International Conference on Medical Image Computing and Computer-Assisted Intervention, Springer. pp. 426–436.
- Haghighi, F., Taher, M.R.H., Zhou, Z., Gotway, M.B., Liang, J., 2021. Transferable visual words: Exploiting the semantics of anatomical patterns for self-supervised learning. *IEEE transactions on medical imaging* 40, 2857–2868.
- Hatamizadeh, A., Tang, Y., Nath, V., Yang, D., Myronenko, A., Landman, B., Roth, H.R., Xu, D., 2022. Unetr: Transformers for 3d medical image segmentation, in: Proceedings of the IEEE/CVF winter conference on applications of computer vision, pp. 574–584.
- He, K., Chen, X., Xie, S., Li, Y., Dollár, P., Girshick, R., 2022. Masked autoencoders are scalable vision learners, in: Proceedings of the IEEE/CVF conference on computer vision and pattern recognition, pp. 16000–16009.
- He, K., Fan, H., Wu, Y., Xie, S., Girshick, R., 2020a. Momentum contrast for unsupervised visual representation learning, in: Proceedings of the IEEE/CVF conference on computer vision and pattern recognition, pp. 9729–9738.
- He, Y., Yang, G., Ge, R., Chen, Y., Coatrieux, J.L., Wang, B., Li, S., 2023. Geometric visual similarity learning in 3d medical image self-supervised pre-training, in: Proceedings of the IEEE/CVF Conference on Computer Vision and Pattern Recognition, pp. 9538–9547.
- He, Y., Yang, G., Yang, J., Chen, Y., Kong, Y., Wu, J., Tang, L., Zhu, X., Dillenseger, J.L., Shao, P., et al., 2020b. Dense biased networks with deep priori anatomy and hard region adaptation: Semi-supervised learning for fine renal artery segmentation. *Medical image analysis* 63, 101722.
- He, Y., Yang, G., Yang, J., Ge, R., Kong, Y., Zhu, X., Zhang, S., Shao, P., Shu, H., Dillenseger, J.L., et al., 2021. Meta grayscale adaptive network for 3d integrated renal structures segmentation. *Medical image analysis* 71, 102055.
- Heimann, T., Van Ginneken, B., Styner, M.A., Arzhaeva, Y., Aurich, V., Bauer, C., Beck, A., Becker, C., Beichel, R., Bekes, G., et al., 2009. Comparison and evaluation of methods for liver segmentation from ct datasets. *IEEE transactions on medical imaging* 28, 1251–1265.
- Huang, W., Li, C., Zhou, H.Y., Yang, H., Liu, J., Liang, Y., Zheng, H., Zhang, S., Wang, S., 2024. Enhancing representation in radiography-reports foundation model: A granular alignment algorithm using masked contrastive learning. *Nature Communications* 15, 7620.
- Isensee, F., Wald, T., Ulrich, C., Baumgartner, M., Roy, S., Maier-Hein, K., Jaeger, P.F., 2024. nnu-net revisited: A call for rigorous validation in 3d medical image segmentation, in: International Conference on Medical Image Computing and Computer-Assisted Intervention, Springer. pp. 488–498.
- Ji, Y., Bai, H., Ge, C., Yang, J., Zhu, Y., Zhang, R., Li, Z., Zhanng, L., Ma, W., Wan, X., et al., 2022. Amos: A large-scale abdominal multi-organ benchmark for versatile medical image segmentation. *Advances in neural information processing systems* 35, 36722–36732.
- Kavur, A.E., Gezer, N.S., Bariş, M., Aslan, S., Conze, P.H., Groza, V., Pham, D.D., Chatterjee, S., Ernst, P., Özkan, S., et al., 2021. Chaos challenge-combined (ct-mr) healthy abdominal organ segmentation. *Medical Image Analysis* 69, 101950.
- Landman, B., Xu, Z., Igelsias, J., Styner, M., Langerak, T., Klein, A., 2015. Miccai multi-atlas labeling beyond the cranial vault—workshop and challenge, in: Proc. MICCAI Multi-Atlas Labeling Beyond Cranial Vault—Workshop Challenge, p. 12.
- Lay, N., Birkbeck, N., Zhang, J., Kevin Zhou, S., 2013. Rapid multi-organ segmentation using context integration and discriminative models, in: International Conference on Information Processing in Medical Imaging, Springer, Berlin, Heidelberg. pp. 450–462.
- Li, S., Zhang, L., Wang, Z., Wu, D., Wu, L., Liu, Z., Xia, J., Tan, C., Liu, Y., Sun, B., et al., 2023. Masked modeling for self-supervised representation learning on vision and beyond. *arXiv preprint arXiv:2401.00897*.
- Li, W., Qu, C., Chen, X., Bassi, P.R., Shi, Y., Lai, Y., Yu, Q., Xue, H., Chen, Y., Lin, X., et al., 2024. Abdomenatlas: A large-scale, detailed-annotated, & multi-center dataset for efficient transfer learning and open algorithmic benchmarking. *Medical Image Analysis* 97, 103285.
- Luo, X., Liao, W., Xiao, J., Chen, J., Song, T., Zhang, X., Li, K., Metaxas, D.N., Wang, G., Zhang, S., 2022. Word: A large scale dataset, benchmark and clinical applicable study for abdominal organ segmentation from ct image. *Medical Image Analysis* 82, 102642.
- Ma, J., Wang, Y., An, X., Ge, C., Yu, Z., Chen, J., Zhu, Q., Dong, G., He, J., He, Z., et al., 2021a. Toward data-efficient learning: A benchmark for covid-19 ct lung and infection segmentation. *Medical physics* 48, 1197–1210.
- Ma, J., Zhang, Y., Gu, S., Ge, C., Ma, S., Young, A., Zhu, C., Meng, K., Yang, X., Huang, Z., et al., 2023. Unleashing the strengths of unlabeled data in pan-cancer abdominal organ quantification: the flare22 challenge. *arXiv preprint arXiv:2308.05862*.
- Ma, J., Zhang, Y., Gu, S., Zhu, C., Ge, C., Zhang, Y., An, X., Wang, C., Wang, Q., Liu, X., et al., 2021b. Abdomenct-1k: Is abdominal organ segmentation a solved problem? *IEEE Transactions on Pattern Analysis and Machine Intelligence* 44, 6695–6714.
- Park, G.Y., Jung, C., Lee, S., Ye, J.C., Lee, S.W., 2024. Self-supervised debiasing using low rank regularization, in: Proceedings of the IEEE/CVF Conference on Computer Vision and Pattern Recognition, pp. 12395–12405.
- Pathak, D., Krahenbuhl, P., Donahue, J., Darrell, T., Efros, A.A., 2016. Context encoders: Feature learning by inpainting, in: Proceedings of the IEEE conference on computer vision and pattern recognition, pp. 2536–2544.
- Podobnik, G., Strojjan, P., Peterlin, P., Ibragimov, B., Vrtovec, T., 2023. Han-seg: The head and neck organ-at-risk ct and mr segmentation dataset. *Medical physics* 50, 1917–1927.
- Rister, B., Yi, D., Shivakumar, K., Nobashi, T., Rubin, D.L., 2020. Ct-org, a new dataset for multiple organ segmentation in computed tomography. *Scientific Data* 7, 381.
- Ronneberger, O., Fischer, P., Brox, T., 2015. U-net: Convolutional networks for biomedical image segmentation, in: Medical image computing and computer-assisted intervention—MICCAI 2015: 18th international conference, Munich, Germany, October 5-9, 2015, proceedings, part III 18, Springer. pp. 234–241.
- Roth, H., Farag, A., Turkbey, E.B., Lu, L., Liu, J., Summers, R.M., 2016. Data from pancreas-ct. The Cancer Imaging Archive.
- Roy, O., Vetterli, M., 2007. The effective rank: A measure of effective dimensionality, in: 2007 15th European signal processing conference, IEEE. pp. 606–610.
- Roy, S., Koehler, G., Ulrich, C., Baumgartner, M., Petersen, J., Isensee, F., Jaeger, P.F., Maier-Hein, K.H., 2023. Mednext: transformer-driven scaling of convnets for medical image segmentation, in: International Conference on Medical Image Computing and Computer-Assisted Intervention, Springer. pp. 405–415.
- Setio, A.A.A., Traverso, A., De Bel, T., Berens, M.S., Van Den Bogaard, C., Cerello, P., Chen, H., Dou, Q., Fantacci, M.E., Geurts, B., et al., 2017. Validation, comparison, and combination of algorithms for automatic detection of pulmonary nodules in computed tomography images: the luna16 challenge. *Medical image analysis* 42, 1–13.
- Shao, P., Qin, C., Yin, C., Meng, X., Ju, X., Li, J., Lv, Q., Zhang, W., Xu, Z., 2011. Laparoscopic partial nephrectomy with segmental renal artery clamping: technique and clinical outcomes. *European urology* 59, 849–855.
- Shao, P., Tang, L., Li, P., Xu, Y., Qin, C., Cao, Q., Ju, X., Meng, X., Lv, Q., Li, J., et al., 2012. Precise segmental renal artery clamping under the guidance of dual-source computed tomography angiography during laparoscopic partial nephrectomy. *European urology* 62, 1001–1008.
- Taleb, A., Loetzsch, W., Danz, N., Severin, J., Gaertner, T., Bergner, B., Lippert, C., 2020. 3d self-supervised methods for medical imaging. *Advances in neural information processing systems* 33, 18158–18172.
- Tang, F., Xu, R., Yao, Q., Fu, X., Quan, Q., Zhu, H., Liu, Z., Zhou, S.K., 2024. Hyspark: Hybrid sparse masking for large scale medical image pre-training, in: International Conference on Medical Image Computing and Computer-Assisted Intervention, Springer. pp. 330–340.
- Tang, Y., Yang, D., Li, W., Roth, H.R., Landman, B., Xu, D., Nath, V., Hatamizadeh, A., 2022. Self-supervised pre-training of swin transformers for 3d medical image analysis, in: Proceedings of the IEEE/CVF conference on computer vision and pattern recognition, pp. 20730–20740.
- Tao, X., Li, Y., Zhou, W., Ma, K., Zheng, Y., 2020. Revisiting rubik’s cube: Self-supervised learning with volume-wise transformation for 3d medical image segmentation, in: Medical Image Computing and Computer Assisted Intervention—MICCAI 2020: 23rd International Conference, Lima, Peru, October 4–8, 2020, Proceedings, Part IV 23, Springer. pp. 238–248.
- Tian, K., Jiang, Y., Diao, Q., Lin, C., Wang, L., Yuan, Z., 2023. Designing bert for convolutional networks: Sparse and hierarchical masked modeling. *arXiv preprint arXiv:2301.03580*.
- Wu, L., Zhuang, J., Chen, H., 2024. Voco: A simple-yet-effective volume contrastive learning framework for 3d medical image analysis, in: Proceedings of the IEEE/CVF Conference on Computer Vision and Pattern Recognition, pp. 22873–22882.
- Xie, Y., Zhang, J., Xia, Y., Wu, Q., 2022a. Unimiss: Universal medical self-supervised learning via breaking dimensionality barrier, in: European Conference on Computer Vision, Springer. pp. 558–575.
- Xie, Z., Zhang, Z., Cao, Y., Lin, Y., Bao, J., Yao, Z., Dai, Q., Hu, H., 2022b.

- Simmin: A simple framework for masked image modeling, in: Proceedings of the IEEE/CVF conference on computer vision and pattern recognition, pp. 9653–9663.
- Yang, H., Li, X., Tang, S., Zhu, F., Wang, Y., Chen, M., Bai, L., Zhao, R., Ouyang, W., 2022. Cycle-consistent masked autoencoder for unsupervised domain generalization, in: The Eleventh International Conference on Learning Representations.
- Zhang, C., Zheng, H., Gu, Y., 2023. Dive into the details of self-supervised learning for medical image analysis. *Medical Image Analysis* 89, 102879.
- Zhang, Q., Wang, Y., Wang, Y., 2022a. How mask matters: Towards theoretical understandings of masked autoencoders. *Advances in Neural Information Processing Systems* 35, 27127–27139.
- Zhang, Q., Wang, Y., Wang, Y., 2022b. How mask matters: Towards theoretical understandings of masked autoencoders. *Advances in Neural Information Processing Systems* 35, 27127–27139.
- Zhang, Q., Wang, Y., Wang, Y., 2022c. How mask matters: Towards theoretical understandings of masked autoencoders. *Advances in Neural Information Processing Systems* 35, 27127–27139.
- Zhang, Y., Tan, Z., Yang, J., Huang, W., Yuan, Y., . Matrix information theory for self-supervised learning, in: Forty-first International Conference on Machine Learning.
- Zhou, H.Y., Lu, C., Chen, C., Yang, S., Yu, Y., 2023a. A unified visual information preservation framework for self-supervised pre-training in medical image analysis. *IEEE Transactions on Pattern Analysis and Machine Intelligence* 45, 8020–8035.
- Zhou, L., Liu, H., Bae, J., He, J., Samaras, D., Prasanna, P., 2023b. Self pre-training with masked autoencoders for medical image classification and segmentation, in: 2023 IEEE 20th International Symposium on Biomedical Imaging (ISBI), IEEE. pp. 1–6.
- Zhou, S.K., Greenspan, H., Shen, D., 2023c. Deep learning for medical image analysis. Academic Press.
- Zhou, Z., Sodha, V., Pang, J., Gotway, M.B., Liang, J., 2021. Models genesis. *Medical image analysis* 67, 101840.

Appendix

7. Datasets

Pre-training and downstream datasets. We utilize thirteen datasets (a total of 9,995 CT scans) for pre-training, including BTCV (Landman et al., 2015), Sliver07 (Heimann et al., 2009), CT-ORG (Rister et al., 2020), FLARE’22 (Ma et al., 2023), CHAOS (Kavur et al., 2021), NaH-Seg (Podobnik et al., 2023), KiPA22 (He et al., 2021, 2020b; Shao et al., 2011, 2012), COVID-19 (Ma et al., 2021a), Pancreas-CT (Roth et al., 2016), LiTS (Bilic et al., 2023), AbdomenCT-1k (Ma et al., 2021b), LUNA16 (Setio et al., 2017), and AbdomenAtlasMini 1.0 (Li et al., 2024). Details of the fine-tuning datasets used for downstream tasks are provided in Table S1. Specifically, we fine-tune seven datasets, including BTCV (Landman et al., 2015), Sliver07 (Heimann et al., 2009), CT-ORG (Rister et al., 2020), FLARE’22 (Ma et al., 2023), WORD (Luo et al., 2022), AMOS (Ji et al., 2022), and BraTS 2021 (Baid et al., 2021), for one-shot and varying dataset proportions fine-tuning.

Table S1: Overview of downstream dataset.

Dataset	Modality	Train					Vaild
		full	one-shot	1%	10%	100% (full)	
BTCV	CT	24	1	1	2	24	6
FLARE’22	CT	50	1	1	10	50	50
AMOS	CT/MRI	240	1	2	25	240	120
WORD	CT	100	1	-	-	-	20
Sliver07	CT	16	1	-	-	-	4
CT-ORG	CT	112	1	-	-	-	28
BraTS 21	MRI	1000	1	-	-	-	251

BTCV dataset. The Multi-Atlas Labeling Beyond The Cranial Vault (BTCV) dataset (Landman et al., 2015) consists of 30 abdominal CT scans annotated at the pixel level for 13 organs by interpreters under the supervision of clinical radiologists at Vanderbilt University Medical Center. Following the previous works (Hatamizadeh et al., 2022; Tang et al., 2022; Wu et al., 2024; Chen et al., 2023a), we utilize the same dataset split, *e.g.*, with 24 scans for training and 6 scans for validation, for fair comparison. Additionally, we conduct random training dataset splits with one-shot, 1%, and 10% proportion (as shown in Table S1).

AMOS dataset. The Multi-Modality Abdominal Multi-Organ Segmentation Challenge (AMOS) dataset (Ji et al., 2022) comprises 360 CT and MRI scans annotated for 15 abdominal organs. We adhere to the official split, using 240 samples for training and 120 samples for validation. We conduct random training dataset splits with different settings for one-shot, 1%, and 10% proportion (as shown in Table S1).

FLARE’22 dataset. The FLARE’22 dataset, from the MICCAI 2022 Fast and Low-resource Semi-Supervised Abdominal Organ Segmentation Challenge (Ma et al., 2023), includes 100 annotated CT scans for the segmentation of 13 abdominal organs. We use the official training set of 50 CT scans and validation set of another 50 CT scans from different medical centers (Clark et al., 2013). We conduct random training dataset splits with different settings for one-shot, 1%, 10% proportion (as shown in Table S1).

WORD dataset. The large-scale whole abdominal organ dataset (WORD) dataset (Luo et al., 2022) contains 150 high-resolution CT scans, with 16 pixel-level organ annotations. We used the

Table S2: Overview of pre-training and fine-tuning settings.

<i>Pre-training pre-processing</i>	
Spacing	$1.5 \times 1.5 \times 1.5$ (mm)
Intensity	[-175, 250]
Sub-volume size	$96 \times 96 \times 96$
Sub-crops	8
Augmentation	Random Rotate, Flip, Scale, Shift
<i>Pre-training settings</i>	
Pre-training steps	400K
Optimizer	AdamW
Weight decay	0.05
Optimizer momentum	$\beta_1, \beta_2 = 0.9, 0.95$
Optimizer LR	$1e-4$
Batch size	$24 \times 8 = 192$
LR schedule	warmup cosine
Warm-up steps	4K
<i>Fine-tuning pre-processing</i>	
Spacing	$1.5 \times 1.5 \times 1.5$ (mm)
Intensity	[-175, 250]
Sub-volume size	$96 \times 96 \times 96$
Sub-crops	4
Augmentation	Random Rotate, Flip, Scale, Shift
<i>Fine-tuning settings</i>	
Optimizer	AdamW
Optimizer LR	$1e-4$
Weight decay	$1e-5$
Batch size	$1 \times 4 = 4$
Swin batch size	1
Inference	sliding window

official training set of 100 CT scans and 20 CT scans for validation (Luo et al., 2022). The WORD dataset is only utilized for the one-shot downstream task (as shown in Table S1).

Sliver07 dataset. The Sliver07 dataset (Heimann et al., 2009), from the Segmentation of Liver Competition held in MICCAI 2007, comprises 20 CT scans for liver segmentation. We adopt an 80/20 train-validation split for the one-shot downstream task (as shown in Table S1).

CT-ORG dataset. The CT volumes with multiple organ segmentations (CT-ORG) dataset (Rister et al., 2020) consists of 150 CT scans for the 5 organ and bone annotations from several clinical sites. We adopt an 80/20 train-validation split for the one-shot downstream task (as shown in Table S1).

BraTS 21 dataset. The BraTS 21 dataset (Baid et al., 2021), from the BraTS 2021 challenge of brain tumors by providing 1251 MRI scans with pixel-level annotations. Following the previous works (Tang et al., 2022; Wu et al., 2024), we utilize the same dataset split, *e.g.*, with 1000 scans for training and 251 scans for validation, for fair comparison. In this paper, we evaluate the ability of model generalization on the BraTs 21 dataset through one-shot fine-tuning.

8. Implementation Details

Pre-training and fine-tuning settings. The details of our pre-training and fine-tuning settings are shown in Table S2. For pre-training task, We sample the pre-training sub-volumes of $96 \times 96 \times 96$ voxels by ratios of positive and negative as 3:1 in 8 sub-crops. Augmentation probabilities for random flip, rotation, intensities scaling, and shifting are set to 0.5, 0.3, 0.1, 0.1, respectively. For downstream task, the sample ratios of positive and negative are as 1:1 in 4 sub-crops. Augmentation

Table S3: Hi-End-MAE variants.

Encoder						
variants	ViT-B/16 ⁽⁷⁶⁸⁾		ViT-B/16 ⁽¹⁵³⁶⁾		ViT-B/12 ⁽¹⁵³⁶⁾	
-	SelfAttn, p. sz. 16, dim 768, head 16	× 12	SelfAttn, p. sz. 16, dim 1536, head 16	× 12	SelfAttn, p. sz. 12, dim 1536, head 16	× 12
Decoder						
-	SelfAttn, p. sz. 16, dim 384, head 16	× 2	SelfAttn, p. sz. 16, dim 528, head 16	× 2	SelfAttn, p. sz. 12, dim 528, head 16	× 2
stage1	CrossAttn, p. sz. 16, dim 384, head 16	× 1	CrossAttn, p. sz. 16, dim 528, head 16	× 1	CrossAttn, p. sz. 12, dim 528, head 16	× 1
stage2	CrossAttn, p. sz. 16, dim 384, head 16	× 1	CrossAttn, p. sz. 16, dim 528, head 16	× 1	CrossAttn, p. sz. 12, dim 528, head 16	× 1
stage3	CrossAttn, p. sz. 16, dim 384, head 16	× 1	CrossAttn, p. sz. 16, dim 528, head 16,	× 1	CrossAttn, p. sz. 12, dim 528, head 16	× 1

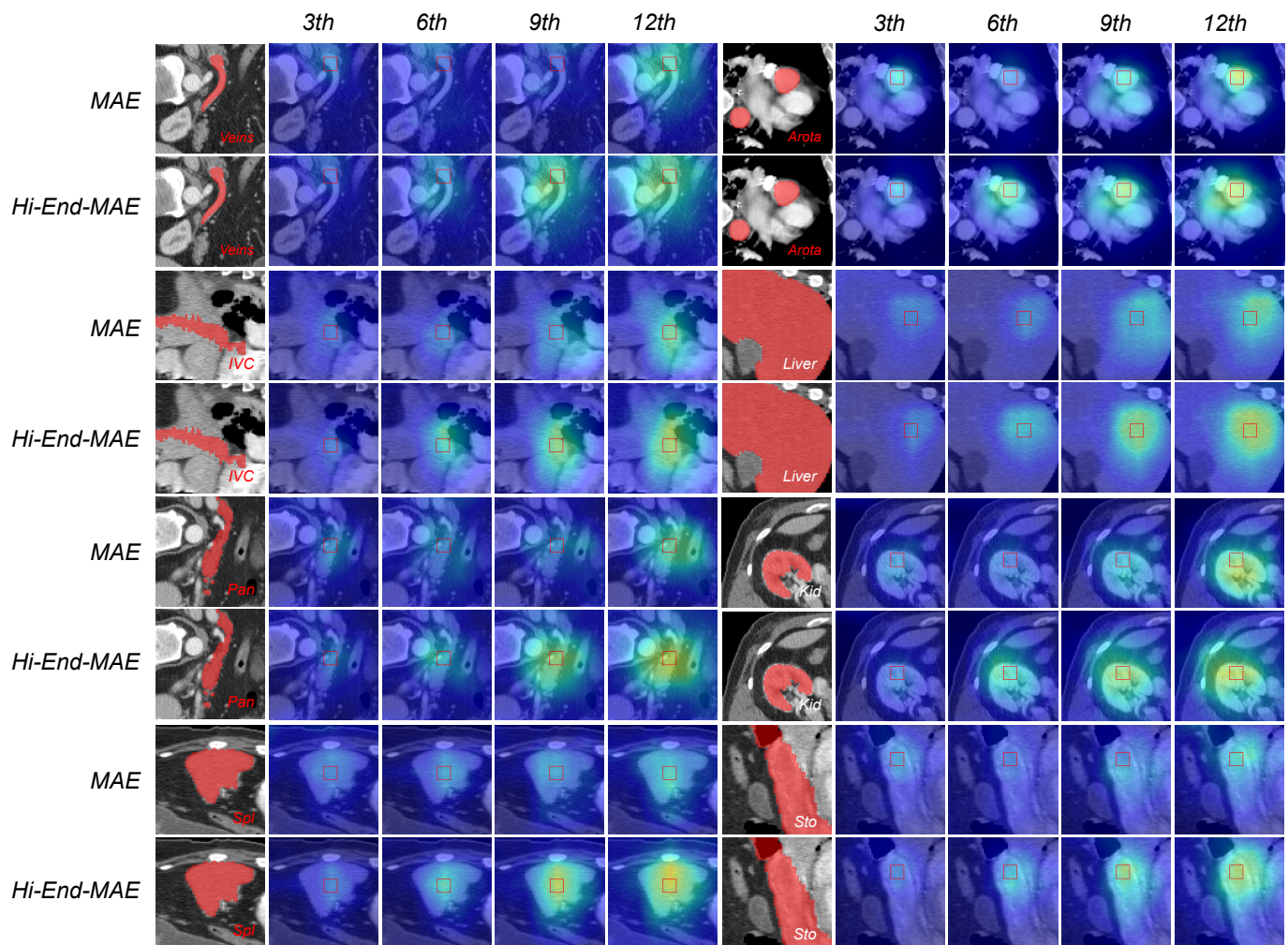


Fig. S1: Visualization of attention maps in the 3th, 6th, 9th, and 12th layers of ViT-B/12⁽¹⁵³⁶⁾ for query patches (red box) on different organs, pre-trained by MAE and Hi-End-MAE. The attention maps are averaged across all attention heads. The abbreviations IVC, Pan, Kid, Spl, and Sto correspond to Inferior Vena Cava, Pancreas, Kidney, Spleen, and Stomach, respectively.

probabilities for random flip, rotation, intensities scaling, and shifting are set to 0.2, 0.2, 0.1, 0.1, respectively. The training epochs for fine-tuning are set to 5000, 5000, 2000, 1000 for one-shot, 1%, 10%, 100% proportion downstream segmentation

tasks, respectively.

Hi-End-MAE variants. The detailed Hi-End-MAE variants are shown in Table S3. “SelfAttn” and “CrossAttn” denote the self attention block and cross attention block, respectively. “p. sz.

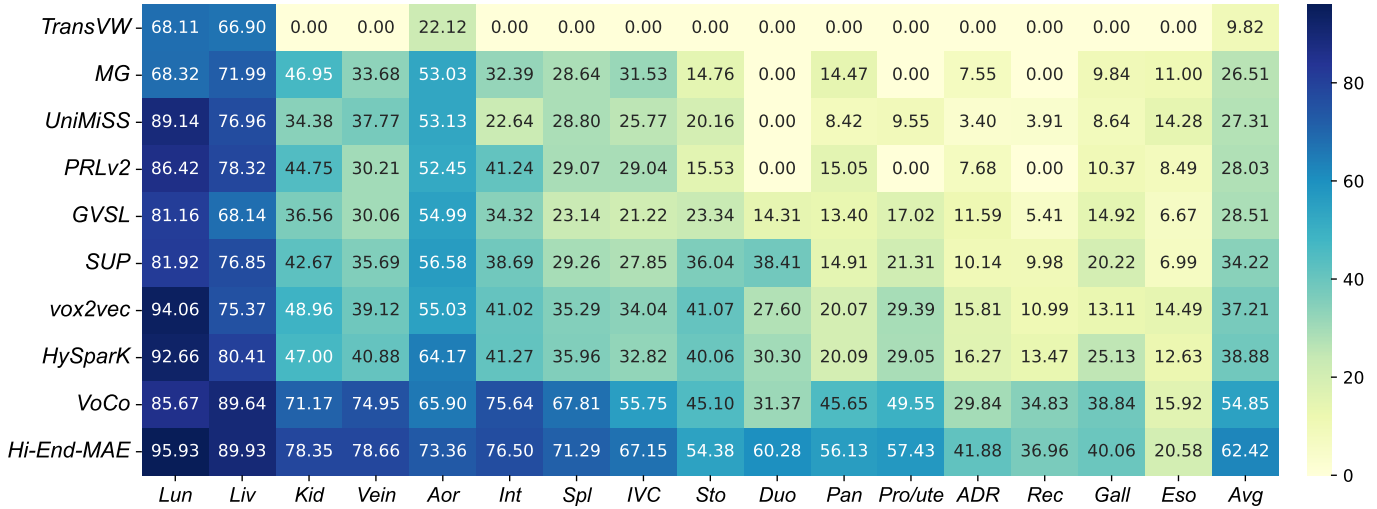


Fig. S2: Comparative analysis one-shot segmentation results across 16 targets in terms of DSC (%) performance.

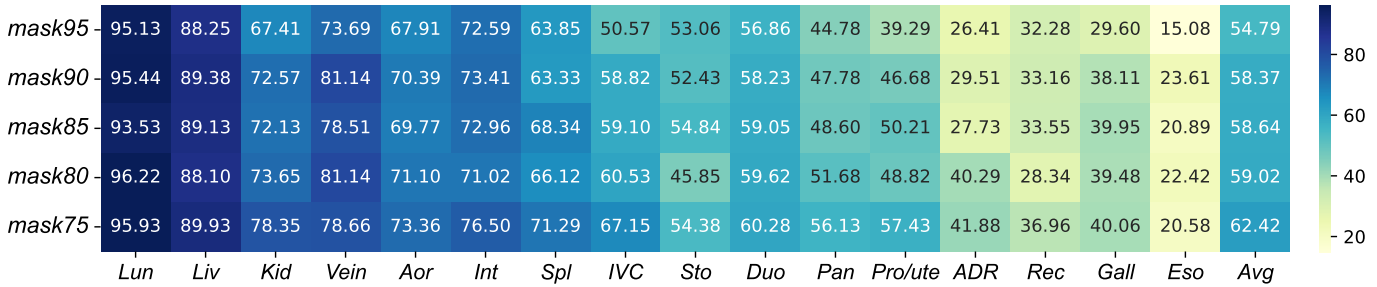


Fig. S3: Comparative analysis of different mask ratios results across 16 segmentation targets in terms of DSC (%) performance.

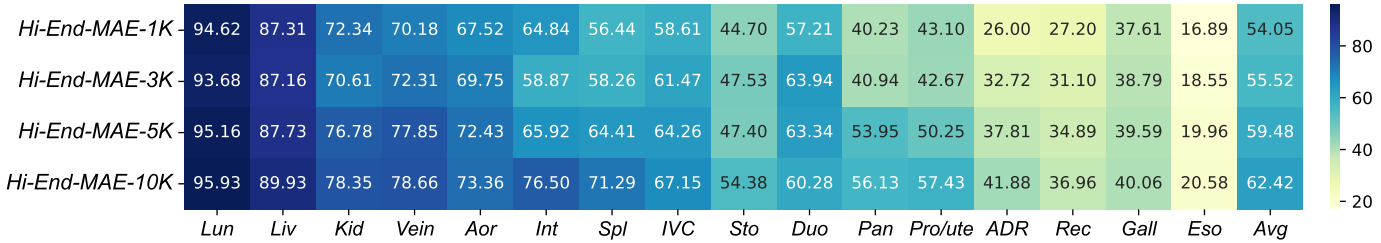


Fig. S4: Comparative analysis of different data scale results across 16 segmentation targets in terms of DSC (%) performance.

12" indicates the patch size of $12 \times 12 \times 12$.

9. Analysis

Local attention patterns. We visualize the slice-level multi-head average attention map from different ViT layers. As shown in Fig.S1, compared to MAE (decoder-driven reconstruction), our Hi-End-MAE benefits from a more refined encoder-driven dense decoding mechanism that learns localized anatomical representations with stronger perceptual capabilities, which could gain the ability to model complex relationships representation.

10. Experiments

Target-specific analysis for one-shot medical segmentation.

We present the average one-shot segmentation semantic results across six datasets, *e.g.*, BTCV (Landman et al., 2015), CT-ORG (Rister et al., 2020), Sliver07 (Heimann et al., 2009), WORD (Luo et al., 2022), AMOS (Ji et al., 2022), and

FLARE'22 (Ma et al., 2023). The overall results are illustrated in Table S2. Hi-End-MAE delivers outstanding one-shot segmentation performance across segmentation targets of varying scales, *e.g.*, achieving a notable improvement in kidney with 7.18%, Arota with 7.46%, Inferior Vena Cava with 11.4%, Stomach with 9.28%, Duodenum with 21.87%, Pancreas with 10.48%, Prostate/Uterus with 7.88%, and Adrenal Gland with 12.04%.

Comparison across various data proportions. We fine-tune pre-trained models on BTCV (Landman et al., 2015), AMOS (Ji et al., 2022) and FLARE'22 (Ma et al., 2023) using 1%, 10%, and 100% proportion of the dataset. The DSC scores of different segmentation targets are shown in Table S4, Table S5, and Table S6, respectively. Our method demonstrates a significant advantage in downstream tasks, particularly in scenarios with limited annotation.

Target-specific analysis for mask ratios and data scales. We present the average one-shot segmentation semantic results across varying mask ratios and data scales on six datasets: BTCV (Landman et al., 2015), CT-ORG (Rister et al., 2020),

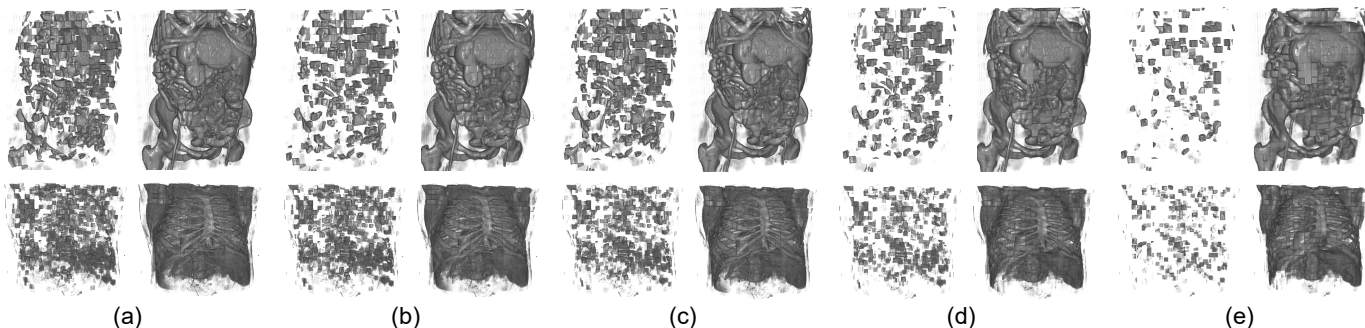


Fig. S5: Abdomen (row 1) and Lung (row 2) CT reconstruction results of Hi-End-MAE with different mask ratios: (a) mask 80% (b) mask 85% (c) mask 85% (d) mask 90% and (e) mask 95%. For each double, we show the masked image (left), and our Hi-End-MAE reconstruction result (right).

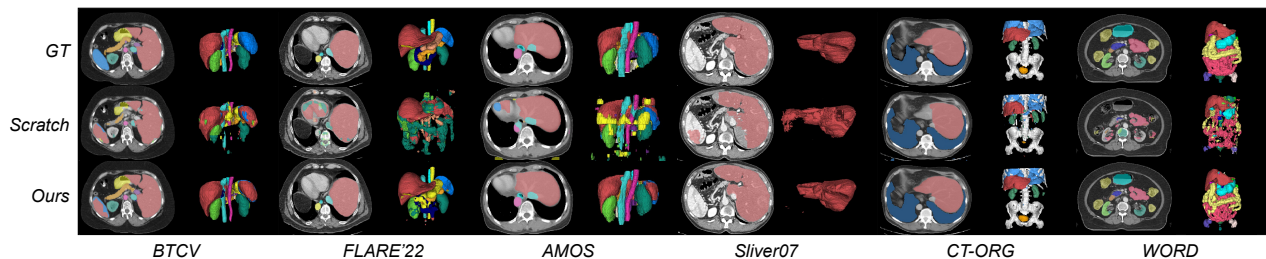


Fig. S6: Qualitative visualization of one-shot segmentation results on BTCV (Landman et al., 2015), FLARE'22 (Ma et al., 2023), AMOS (Ji et al., 2022), Sliver07 (Heimann et al., 2009), CT-ORG (Rister et al., 2020), and WORD (Luo et al., 2022). Left/Right: Slice/Volume segmentation results on the same dataset.

Sliver07 (Heimann et al., 2009), WORD (Luo et al., 2022), AMOS (Ji et al., 2022), and FLARE'22 (Ma et al., 2023). The specific segmentation target results on different mask ratios and data scales are shown in Fig.S3 and Fig.S4, respectively.

11. Visualization

Reconstruction visualization. We visualize 3D reconstruction results to check what Hi-End-MAE learns in pre-training with different mask ratios. As shown in Fig.S5, our method can almost reconstruct the different shapes of organs, bones, and other details from the very small portion of unmasked patches.

More segmentation result visualization. Visualization results on BTCV (Landman et al., 2015), CT-ORG (Rister et al., 2020), Sliver07 (Heimann et al., 2009), WORD (Luo et al., 2022), AMOS (Ji et al., 2022), and FLARE'22 (Ma et al., 2023) are shown in Fig.S6. It can be observed that, compared to training from scratch, the high-quality representations learned by Hi-End-MAE provide significant benefits to downstream tasks.

Table S4: Comparison of different methods with 1%, 10%, and 100% proportions on BTCV (Landman et al., 2015). We report the DSC (%) performance. **val** (bold) / yal (underline) : top method / second method. † denotes we utilize official pre-training weights. ‡ denotes the results are copied from (Wu et al., 2024). The abbreviations Spl, RKid, LKid, Gall, Eso, Liv, Sto, Aor, IVC, Veins, Pan, RAG, and LAG correspond to Spleen, Right kidney, Left kidney, Gallbladder, Esophagus, Liver, Stomach, Aorta, Inferior Vena Cava, Veins, Pancreas, Right Adrenal Gland, and Left Adrenal Gland, respectively.

Method	BTCV (100%)													Avg
	Spl	RKid	LKid	Gall	Eso	Liv	Sto	Aor	IVC	Veins	Pan	RAG	LAG	
<i>From scratch</i>														
UNETR†‡	93.02	94.13	94.12	66.99	70.87	96.11	77.27	89.22	82.10	70.16	76.65	65.32	59.21	79.82
SwinUNETR†‡	94.06	93.54	93.80	65.51	74.60	97.09	75.94	91.80	82.36	73.63	75.19	68.00	61.11	80.53
<i>Medical SSL</i>														
MG†‡	91.99	93.52	91.81	65.11	76.14	95.98	<u>86.88</u>	89.29	83.59	71.79	81.62	67.97	63.18	81.45
PRLv2†‡	95.50	91.43	89.52	76.15	73.54	<u>97.28</u>	79.64	90.16	84.17	75.20	78.71	68.74	62.93	81.74
SUP†‡	95.25	93.16	92.97	63.62	73.96	96.21	79.32	89.98	83.19	76.11	<u>82.25</u>	68.99	65.11	81.54
GVSL†‡	95.27	91.22	92.25	72.69	73.56	96.44	82.40	88.90	84.22	70.84	76.42	67.48	63.25	81.87
VoCo†‡	<u>95.73</u>	96.53	94.48	<u>76.02</u>	75.60	97.41	78.43	<u>91.21</u>	<u>86.12</u>	78.19	80.88	71.47	<u>67.88</u>	<u>83.85</u>
Hi-End-MAE	96.33	<u>94.87</u>	94.87	64.55	<u>75.72</u>	97.16	91.80	90.64	86.91	<u>78.16</u>	85.68	<u>70.44</u>	71.79	84.53
<i>BTCV (10%)</i>														
<i>From scratch</i>														
UNETR	60.25	76.85	64.96	30.47	41.77	86.73	22.01	63.15	48.58	39.90	22.28	0.00	0.00	42.85
SwinUNETR	81.59	80.86	79.78	36.48	37.55	88.96	25.41	57.90	57.99	49.20	12.05	43.98	15.49	51.33
<i>General SSL</i>														
SparK	69.60	60.61	55.83	35.04	26.46	88.47	37.67	67.96	60.59	52.86	30.73	49.42	31.11	51.26
MAE	86.87	92.64	92.75	47.09	60.17	95.00	71.69	86.37	<u>81.96</u>	<u>68.51</u>	74.23	59.96	57.81	75.01
<i>Medical SSL</i>														
MG†	59.10	62.29	52.00	24.28	0.00	82.92	36.49	69.95	62.16	45.13	0.143	0.00	0.00	38.04
TransVW†	0.00	0.00	0.00	0.00	0.00	81.23	28.21	0.00	0.00	0.00	0.00	0.00	0.00	8.42
UniMiSS†	48.47	74.86	72.64	25.82	30.56	88.62	28.38	59.93	56.67	53.93	39.00	33.15	0.00	47.08
SUP	64.41	76.44	70.29	30.90	33.36	86.85	24.78	64.86	57.66	54.66	16.47	37.82	27.14	49.67
PRLv2†	71.98	62.80	46.66	0.00	0.00	88.37	19.14	57.99	49.34	0.00	0.00	0.00	0.00	30.48
GVSL†	52.82	33.54	34.05	35.44	41.98	90.91	33.14	74.80	44.95	34.78	18.86	25.83	22.06	41.79
vox2vec†	65.02	71.73	68.90	22.30	33.50	90.44	36.57	73.32	62.13	44.02	39.28	43.07	22.70	51.77
HySparK†	58.79	61.56	57.58	45.76	29.77	89.95	43.40	68.37	60.33	52.28	19.50	48.15	34.55	51.54
VoCo†	<u>91.73</u>	<u>92.83</u>	<u>93.18</u>	65.13	67.60	95.58	78.76	<u>86.81</u>	78.18	66.58	71.05	64.53	59.98	<u>77.85</u>
Hi-End-MAE	92.31	93.47	93.46	<u>63.56</u>	<u>66.14</u>	96.03	79.97	88.74	83.66	69.98	<u>71.84</u>	<u>62.40</u>	<u>59.64</u>	78.56
<i>BTCV (1%)</i>														
<i>From scratch</i>														
UNETR	30.60	49.93	35.31	4.555	28.35	83.21	13.72	39.16	30.01	23.52	6.042	14.26	5.923	28.05
SwinUNETR	25.76	41.29	21.58	10.84	27.85	80.97	14.03	49.00	40.43	20.23	1.995	25.96	0.189	27.71
<i>General SSL</i>														
SparK	41.65	41.08	40.09	9.036	25.79	81.29	15.17	52.37	38.45	19.47	3.298	19.64	11.62	30.69
MAE	71.68	87.19	87.68	<u>21.58</u>	55.09	88.96	53.41	80.81	<u>73.27</u>	<u>58.41</u>	<u>49.00</u>	47.39	32.02	62.04
<i>Medical SSL</i>														
MG†	45.95	32.98	46.88	0.00	0.00	74.28	15.31	69.50	47.15	45.20	3.174	0.00	0.00	29.27
TransVW†	0.00	0.00	0.00	0.00	0.00	73.25	0.00	0.00	0.00	0.00	0.00	0.00	0.00	5.634
UniMiSS†	49.62	58.16	52.88	1.752	21.68	80.67	16.30	53.55	41.77	27.05	3.741	15.06	6.044	32.95
SUP†	20.14	45.41	37.65	8.281	29.73	81.66	13.50	51.83	35.21	20.28	0.098	26.72	3.141	28.74
PRLv2†	42.37	25.11	46.39	0.00	0.00	82.12	14.19	48.80	35.12	17.89	0.041	0.00	0.00	24.01
GVSL†	36.48	18.09	22.78	2.828	17.84	76.21	11.83	53.68	32.21	29.14	4.923	16.71	0.481	24.86
vox2vec†	52.08	30.36	37.30	10.92	43.86	86.65	14.72	66.05	47.59	27.99	5.075	32.91	3.176	35.29
HySparK†	36.77	38.86	48.45	17.83	41.83	79.53	17.91	63.49	39.71	34.71	1.399	25.31	19.66	35.81
VoCo†	<u>83.61</u>	89.17	90.66	20.56	<u>60.38</u>	<u>91.80</u>	<u>61.94</u>	<u>83.04</u>	70.03	50.98	14.01	56.76	50.32	<u>63.33</u>
Hi-End-MAE	85.55	<u>87.22</u>	<u>89.00</u>	24.43	67.78	93.48	72.22	84.03	74.28	64.02	61.83	<u>53.28</u>	<u>47.51</u>	69.59

Table S5: Comparison of different methods with 1%, 10%, and 100% proportions on AMOS (Ji et al., 2022). We report the DSC (%) performance. **val** (bold) / val (underline) : top method / second method. † denotes we utilize official pre-training weights. The abbreviations Spl, RKid, LKid, Gall, Eso, Liv, Sto, Aor, IVC, Pos, Pan, RAG, LAG, Duo, Bla and Pro/Ute correspond to Spleen, Right kidney, Left kidney, Gallbladder, Esophagus, Liver, Stomach, Aorta, Postcava, Pancreas, Right Adrenal Gland, Left Adrenal Gland, Duodenum, Bladder, and Prostate/Uterus, respectively.

Method	AMOS (100%)															Avg
	Spl	RKid	LKid	Gall	Eso	Liv	Sto	Aor	Pos	Pan	RAG	LAG	Duo	Bla	Pro/Ute	
<i>From scratch</i>																
UNETR	93.20	90.66	92.22	66.04	71.90	95.31	82.07	90.31	82.18	74.91	65.87	63.65	63.88	63.52	59.61	77.02
SwinUNETR	95.26	93.34	94.35	75.95	79.02	96.71	88.10	93.11	87.70	82.92	70.80	71.20	75.12	69.14	64.96	82.51
<i>General SSL</i>																
SparK	95.64	93.71	95.23	<u>78.50</u>	80.98	97.01	91.30	93.71	88.92	84.65	71.65	73.59	77.92	72.70	65.58	84.07
MAE	95.94	93.83	95.24	75.57	80.02	97.16	90.43	93.53	88.28	84.33	72.19	71.65	76.97	72.55	66.54	83.61
<i>Medical SSL</i>																
MG†	93.84	91.51	91.92	75.30	0.00	93.82	88.44	93.24	88.22	83.62	0.00	0.00	74.56	70.26	0.00	62.99
TransVW†	94.01	92.12	92.19	74.31	80.36	95.37	88.71	93.23	88.35	83.65	72.18	72.71	76.07	70.46	64.88	82.58
UniMiSS†	94.19	92.40	93.83	71.76	72.73	96.09	86.63	91.43	84.63	79.16	66.52	67.27	70.48	68.90	62.64	79.92
SUP†	95.07	93.40	94.36	75.79	79.22	96.69	88.12	93.05	87.48	82.28	71.25	70.78	74.63	69.13	65.48	82.45
PRLv2†	89.20	87.69	88.14	67.83	0.00	93.97	81.07	91.24	82.02	71.64	0.00	0.00	59.28	0.00	0.00	54.14
GVSL†	94.22	92.46	93.26	73.95	78.63	96.17	87.84	92.36	86.23	81.35	70.25	69.97	73.11	67.91	62.99	81.38
vox2vec†	88.34	89.79	87.54	66.51	69.39	93.62	77.95	90.45	81.41	70.69	63.82	60.58	60.71	64.97	55.85	74.78
HySparK†	<u>96.08</u>	94.43	<u>67.44</u>	95.92	79.59	83.78	97.42	92.22	94.33	90.26	86.29	74.86	76.27	80.43	<u>74.27</u>	85.58
VoCo†	95.57	94.07	95.07	78.42	81.77	96.89	90.66	93.93	89.25	85.37	<u>73.49</u>	74.43	78.52	72.13	66.90	84.44
Hi-End-MAE	96.15	<u>94.09</u>	68.43	<u>95.86</u>	77.18	<u>82.55</u>	<u>97.38</u>	<u>92.17</u>	<u>94.09</u>	<u>89.47</u>	<u>85.74</u>	<u>73.27</u>	<u>74.51</u>	<u>79.18</u>	74.52	<u>84.98</u>
<i>AMOS (10%)</i>																
<i>From scratch</i>																
UNETR	74.37	72.46	70.27	51.47	53.96	79.27	61.19	76.42	66.08	55.37	49.17	37.69	40.12	60.46	52.66	60.06
SwinUNETR	78.14	74.17	70.25	53.80	57.74	82.73	66.29	81.72	69.09	58.55	50.87	41.35	47.74	62.24	56.99	63.45
<i>General SSL</i>																
SparK	86.05	86.31	84.81	59.63	63.71	89.94	75.60	88.59	76.68	67.63	60.43	53.77	60.26	63.60	58.14	71.68
MAE	82.38	<u>86.69</u>	59.09	83.29	60.30	66.69	90.42	<u>77.64</u>	<u>88.43</u>	<u>77.65</u>	72.11	<u>61.61</u>	60.23	<u>60.80</u>	<u>66.79</u>	72.94
<i>Medical SSL</i>																
MG†	74.68	74.87	73.70	0.00	0.00	87.56	66.00	84.86	73.32	60.49	0.00	0.00	45.95	62.61	0.00	46.94
TransVW†	77.81	76.15	74.35	58.29	64.26	87.49	69.98	87.32	75.15	61.11	57.43	44.73	49.64	64.02	55.80	66.91
UniMiSS†	83.35	75.73	78.99	54.28	60.09	89.46	68.40	82.95	69.51	63.04	52.50	48.44	49.80	62.75	55.77	66.34
SUP†	77.34	78.32	73.15	53.70	60.62	82.99	65.53	83.08	70.97	60.16	53.72	46.89	49.74	62.27	55.73	64.95
PRLv2†	73.23	75.92	77.21	0.00	0.00	78.15	66.17	86.40	67.45	0.00	0.00	0.00	0.00	61.52	0.00	39.07
GVSL†	80.09	72.98	73.48	50.58	59.84	81.77	66.17	85.84	70.66	57.79	46.74	43.14	44.66	61.89	56.04	63.45
vox2vec†	75.61	73.14	73.80	52.68	58.05	78.53	67.46	83.21	66.13	57.35	45.79	38.10	47.64	62.37	54.61	62.30
HySparK†	75.71	80.04	74.62	55.63	57.68	82.39	68.85	82.49	72.80	56.21	42.61	45.64	51.13	62.69	56.23	64.32
VoCo†	89.35	81.64	<u>61.57</u>	<u>85.30</u>	<u>62.39</u>	67.95	90.60	76.09	87.83	80.07	<u>72.44</u>	59.47	60.38	60.64	64.27	<u>73.34</u>
Hi-End-MAE	<u>89.07</u>	90.52	63.16	90.20	62.72	<u>67.54</u>	93.26	78.30	87.19	<u>79.59</u>	76.62	62.00	64.11	65.48	67.71	75.84
<i>AMOS (1%)</i>																
<i>From scratch</i>																
UNETR	28.83	21.01	19.53	26.21	11.86	72.55	35.04	33.54	30.53	8.181	5.494	1.366	4.098	33.62	23.16	23.67
SwinUNETR	45.56	29.01	29.87	18.64	20.68	78.89	35.03	48.73	33.12	14.33	11.54	5.242	4.915	36.22	22.40	28.94
<i>General SSL</i>																
SparK	53.92	49.97	48.45	16.12	36.78	71.06	49.10	70.68	42.42	17.81	10.17	11.12	13.77	28.16	22.60	36.14
MAE	67.62	72.90	<u>48.99</u>	75.55	34.95	44.29	86.68	65.72	75.79	63.37	43.95	<u>28.19</u>	44.66	<u>26.48</u>	40.94	54.67
<i>Medical SSL</i>																
MG†	37.00	30.65	30.78	20.77	0.00	75.23	35.12	59.42	39.17	6.713	0.00	0.00	3.910	31.48	15.48	25.72
TransVW†	20.27	26.30	26.51	0.00	0.00	71.11	32.09	54.82	32.16	8.989	0.00	1.640	4.202	0.00	2.670	18.72
UniMiSS†	53.58	34.17	36.66	21.38	16.00	82.24	38.27	38.96	36.36	12.62	3.501	0.811	4.045	35.64	28.08	29.49
SUP†	49.97	28.37	28.83	15.26	18.08	72.88	29.65	38.37	31.34	12.95	11.52	0.00	5.635	16.74	24.29	25.60
PRLv2†	41.59	26.29	26.86	0.00	0.00	70.50	35.64	56.01	34.51	3.044	0.00	0.00	1.375	20.20	0.00	21.07
GVSL†	42.21	20.83	24.83	22.95	22.22	71.36	30.46	46.43	23.93	8.833	4.398	4.964	5.663	20.14	14.52	24.25
vox2vec†	38.43	43.18	20.69	20.53	33.47	72.13	36.21	66.26	42.14	18.09	8.152	10.32	14.75	37.32	29.73	32.76
HySparK†	43.62	43.39	41.82	23.36	26.58	71.66	46.87	67.59	40.93	18.61	7.166	15.85	13.45	31.78	24.76	34.50
VoCo†	72.57	78.74	31.43	<u>79.82</u>	<u>43.08</u>	46.58	85.35	72.39	80.57	<u>63.95</u>	48.63	21.42	<u>43.27</u>	24.44	<u>44.81</u>	55.81
Hi-End-MAE	<u>71.98</u>	<u>74.43</u>	50.71	80.59	45.36	49.97	85.08	<u>70.52</u>	<u>77.40</u>	64.84	54.52	42.48	41.22	41.94	54.15	60.35

Table S6: Comparison of different methods with 1%, 10%, and 100% proportions on FLARE'22 (Ma et al., 2023). We report the DSC (%) performance. **val** (bold) / val (underline) : top method / second method. † denotes we utilize official pre-training weights. The abbreviations Liv, RKid, LKid, Spl, Pan, Aor, IVC, RAG, LAG, Gall, Eso, Sto, and Duo correspond to Liver, Right kidney, Left kidney, Spleen, Pancreas, Aorta, Inferior Vena Cava, Right Adrenal Gland, and Left Adrenal Gland, Gallbladder, Esophagus, Stomach, and Duodenum, respectively.

Method	FLARE'22 (100%)												Avg	
	Liv	RKid	LKid	Spl	Pan	Aor	IVC	RAG	LAG	Gall	Eso	Sto		Duo
<i>From scratch</i>														
UNETR	93.48	78.17	76.43	86.14	63.80	83.44	74.17	64.88	52.07	55.77	69.04	72.44	50.73	70.81
SwinUNETR	94.74	81.59	79.54	87.68	69.38	90.30	80.18	67.99	61.63	57.25	70.99	78.16	60.45	75.38
<i>General SSL</i>														
SparK	96.09	84.12	85.96	91.47	79.64	92.37	83.61	70.22	68.58	62.07	75.90	85.20	73.35	80.67
MAE	96.85	88.12	<u>87.60</u>	92.28	82.87	93.88	<u>86.34</u>	74.56	69.07	64.24	76.66	<u>88.33</u>	72.42	82.56
<i>Medical SSL</i>														
MG†	93.60	71.01	71.53	80.15	71.59	86.49	78.47	0.00	0.00	56.39	0.00	74.24	61.76	57.33
TransVW†	94.20	73.84	72.08	82.39	76.07	88.91	79.30	70.18	65.60	59.71	77.46	80.57	64.69	75.78
UniMiSS†	95.56	75.33	73.44	90.29	72.25	89.90	79.14	68.67	64.98	58.99	66.19	79.33	57.16	74.71
SUP†	94.87	81.85	80.24	87.55	69.92	89.07	78.72	66.60	58.84	57.65	72.53	77.80	58.80	74.96
PRLv2†	83.67	68.04	62.64	74.11	71.04	84.84	74.04	0.00	0.00	51.34	0.00	78.54	57.44	54.29
GVSL†	93.95	73.98	73.36	85.23	71.89	90.55	74.48	67.73	59.81	55.63	69.62	79.44	56.74	73.27
vox2vec†	80.67	75.50	75.42	76.25	73.10	89.93	79.11	59.76	55.73	49.15	67.18	77.91	54.56	70.33
HySparK†	96.45	89.48	87.32	91.96	83.30	93.83	85.19	70.18	<u>71.19</u>	63.38	78.89	85.91	73.39	82.35
VoCo†	96.89	87.76	85.82	<u>92.62</u>	<u>84.32</u>	<u>94.29</u>	85.29	76.93	71.18	<u>64.48</u>	80.04	87.05	73.84	83.12
Hi-End-MAE	97.18	<u>89.29</u>	88.82	93.41	84.84	94.82	87.88	<u>75.85</u>	72.76	65.04	<u>79.03</u>	89.48	76.08	84.20
FLARE'22 (10%)														
<i>From scratch</i>														
UNETR	88.78	63.45	62.53	61.20	48.54	78.70	58.17	53.17	33.78	38.22	60.25	53.91	33.35	56.46
SwinUNETR	90.69	65.45	58.83	74.18	57.45	82.37	66.39	59.35	50.36	48.64	65.67	58.38	46.16	63.38
<i>General SSL</i>														
SparK	94.07	74.01	74.38	84.75	73.61	89.80	76.68	60.29	57.00	51.34	68.88	72.17	55.54	71.74
MAE	95.20	76.51	78.72	86.12	79.22	92.96	82.20	67.23	62.15	<u>60.19</u>	73.32	79.07	<u>68.17</u>	77.01
<i>Medical SSL</i>														
MG†	88.57	57.05	54.98	70.38	55.78	84.82	66.29	0.00	0.00	44.33	0.00	59.50	44.65	48.18
TransVW†	89.12	53.34	51.98	62.48	63.55	83.74	70.33	58.24	46.88	47.35	66.34	64.35	49.08	62.07
UniMiSS†	90.40	68.55	61.09	68.87	55.41	82.96	63.74	56.52	50.02	44.89	57.56	56.12	36.73	60.99
SUP†	89.69	63.82	55.83	63.15	55.51	81.64	66.68	55.83	40.97	48.45	64.63	56.79	41.44	60.35
PRLv2†	89.39	56.33	47.00	58.86	51.86	84.18	68.90	0.00	0.00	0.00	0.00	64.37	37.65	42.97
GVSL†	90.40	59.04	58.52	71.19	53.54	80.32	62.90	53.12	38.90	48.11	56.05	60.39	41.45	59.54
vox2vec†	90.60	65.40	56.22	65.36	61.83	81.13	69.34	54.50	41.50	49.75	64.28	60.11	45.84	61.99
HySparK†	94.59	75.05	74.70	87.15	73.25	90.84	77.03	69.03	59.52	53.80	74.05	69.31	58.41	73.60
VoCo†	<u>96.37</u>	<u>80.70</u>	<u>81.24</u>	<u>89.06</u>	<u>80.28</u>	<u>93.28</u>	<u>82.45</u>	72.89	67.15	59.73	77.75	<u>80.02</u>	63.89	<u>78.84</u>
Hi-End-MAE	96.53	84.60	82.82	92.67	82.40	93.85	85.25	69.57	<u>65.17</u>	61.90	<u>76.39</u>	83.74	72.64	80.58
FLARE'22 (1%)														
<i>From scratch</i>														
UNETR	79.55	33.05	21.85	45.32	14.27	46.34	27.78	4.215	0.00	20.79	24.23	20.49	3.979	26.30
SwinUNETR	80.45	45.22	37.37	45.01	21.44	63.45	45.46	13.36	7.671	31.44	27.47	31.90	16.26	35.89
<i>General SSL</i>														
SparK	83.63	41.92	32.04	48.15	22.89	58.12	44.64	9.142	13.18	23.97	33.74	43.18	19.62	36.48
MAE	88.87	72.24	<u>59.91</u>	70.86	61.85	88.75	<u>70.75</u>	44.77	46.96	34.47	<u>59.08</u>	<u>66.80</u>	<u>45.21</u>	<u>62.35</u>
<i>Medical SSL</i>														
MG†	72.64	33.54	34.72	39.79	16.10	61.64	38.19	0.00	0.00	20.60	0.00	29.48	8.115	27.30
TransVW†	62.50	0.00	0.00	0.00	0.00	0.00	0.00	0.00	0.00	0.00	0.00	0.00	0.00	4.807
UniMiSS†	72.90	35.59	24.13	22.31	19.10	40.34	21.63	0.00	5.034	24.43	15.66	33.80	9.015	24.92
SUP†	83.17	38.20	34.70	52.42	20.88	59.71	39.53	5.548	10.33	25.23	23.94	31.95	12.67	33.72
PRLv2†	80.31	33.82	20.32	46.03	18.92	65.71	43.38	0.00	0.00	20.29	0.00	25.18	6.190	27.71
GVSL†	75.57	26.34	26.64	41.81	14.15	47.10	24.30	2.690	0.00	22.09	18.12	28.99	14.45	26.33
vox2vec†	69.73	33.29	33.66	37.72	29.60	58.24	46.40	6.671	8.964	19.83	40.53	35.47	23.25	34.11
HySparK†	83.07	43.34	37.74	51.38	22.88	66.24	47.03	15.03	4.253	31.27	25.19	37.11	23.47	37.54
VoCo†	91.21	59.29	66.63	78.29	50.82	79.31	66.23	31.61	35.00	41.35	50.40	62.52	36.85	57.66
Hi-End-MAE	<u>90.29</u>	<u>71.13</u>	59.75	<u>71.77</u>	<u>61.66</u>	<u>86.03</u>	74.62	<u>43.34</u>	46.96	<u>34.97</u>	59.54	71.26	50.61	63.22